THEORETICAL AND APPLIED ENGINEERING

Universidade Federal de Lavras
Departamento de Engenharia

EDITORA UFLA
UNIVERSIDADE FEDERAL DE LAVRAS

Theoretical And Applied Engineering

THEORETICAL AND APPLIED ENGINEERING, LAVRAS, V1, N1, P. 1-37, JAN/MAR. 2017

Theoretical and Applied Engineering is edited quarterly by the Federal University of Lavras Publisher (Editora UFLA) and covers all aspects and information on scientific and technical advances in the engineering sciences. Theoretical and Applied Engineering is devoted to a wide range of subfields in the engineering sciences and interdisciplinary articles are particularly welcome.

AVAILABLE ON THE WEB

http://www.taae.deg.ufla.br/taae/index.php/TAAE/index

MAILING ADDRESS

Engineering Department/DEG,
Campus of the Federal University of Lavras/UFLA
Post Office Box 3037 - 37200-000 - Lavras, MG - Brazil
E-mail: taaeufla@gmail.com
Homepage: http://www.deg.ufla.br/

Cataloguing data elaborated by the Coordination of Technical Processes of the University Library

Theoretical and Applied Engineering [electronic resource] /
Federal University of Lavras, Engineering Department –
Vol. 1, n. 1 (jan./mar. 2017)- . – Digital. – Lavras:
UFLA, 2017- .
v. 1, n. 1. (2017)-

Quarterly
eISSN: 2594-3863

1. Engineering. 2 Science. 3. Technology. I. Federal University of Lavras, Engineering Department. II. Title.

CDD – 620

Indexed in
Google Scholar

THEORETICAL AND APPLIED ENGINEERING

THEORETICAL AND APPLIED ENGINEERING
v. 1, n. 1, January/March 2017

TABLE OF CONTENTS

EVALUATION OF THE OPERATIONAL VIABILITY OF THE USE OF ELECTRICITY AS A SOURCE OF POWER IN AGRICULTURAL TRACTORS

Vanderson Rabelo de Paula
Instituto Federal Sul de Minas/IFSULDEMINAS, Departamento de Engenharia Agrícola, Machado, MG, Brazil
Corresponding author: E-mail: Vanderson.paula@ifsuldeminas.edu.br

Carlos Eduardo da Silva Volpato
Universidade Federal de Lavras/UFLA, Departamento de Engenharia/DEG, Lavras, MG, Brazil

Jackson Antônio Barbosa
Universidade Federal de Lavras/UFLA, Departamento de Engenharia/DEG, Lavras, MG, Brazil

Abstract: Economic and environmental problems caused by more than a century of intense use of fuels derived from petroleum have led to a constant search for alternative sources of energy, ether in urban areas or in the agricultural environment. In this context, the aim of this study was to evaluate the operational viability of the use of electricity as an energy source for agricultural tractors. For that, comparison of performance curves between internal combustion engine, used in agricultural tractor, and an electrical motor has been made. The electrical motor performance was considered in the proposal a theoretical set up of an electrical tractor. The hypothesis was evaluated considering its autonomy in different power demands and compared to a conventional farm tractor regarding to operating energy cost and energy efficiency. The electrical motor presented the best results for torque, power, energy efficiency and operational energetic cost. The autonomy of theoretical configuration was superior then eight hours per day, for medium and lower power, working in lower rotations. Considering these results, it was possible to conclude that the use of electricity as an energy source for agricultural tractors is viable in terms of cost and energy efficiency and has potential for intensification of research in this field.

Keywords: Agricultural mechanization; energetic efficiency; alternative energy; sustainability.

Received: April, 14, 2016 - Accepted: January, 06, 2017

INTRODUCTION

According to Armstrong (2000) agricultural mechanization is the seventh greatest invention of the twentieth century, overcome the computer, phone and spacecraft.

According to Steckel and White (2012), the efficiency of agricultural tractors in mechanized operations has dramatically reduced the necessary inputs in food production. However, according to Serrano (2007), the tractors are selected to supply the needs of implements with high power demand, which often leads to oversize the tractor in relation to implements that require less power.

Volpato et al. (2009) conducted performance tests on a tractor in which observed that as the required traction strength decreased, the tractor passes to an oversized condition and thus, there is a significant increase in specific fuel consumption. According to Silveira and Sierra (2010) for comparative estimates, the energy efficiency using the average specific fuel consumption in liters per kilowatt-hour (kWh L^{-1}), was based on the most frequent sites of use of the tractor engine. Thus, it can be said that in oversized tractors, energy efficiency becomes even lower.

According to Mousazadeh et al. (2010), the energy issue, agricultural tractors have great contribution portion for air pollution. US Environmental Protection Agency (USEPA, 2012) off-road vehicles such as agricultural tractors, are responsible for 15-20% of air pollution in US. Based on economic and environmental problems caused by the massive dependence on fossil fuels is that the automobile industry has been interested in development of vehicles that use alternative sources of energy, such as electric and hybrid vehicles.

Mousazadeh et al. (2010) the government of Barack Obama, in the United States, set a goal of one million electric vehicles circulating in its highways by 2015. A series of patents on electric tractors, as required by Edmond (2006) show that the concern in using renewable energy sources is not limited to road vehicles but also extending to other types of vehicles, such as agricultural tractors.

In this context the aim of this research was to evaluate the operational viability of the use of electricity as a source of power in agricultural tractors, determining and comparing its operating costs with internal combustion engine used in a conventional tractor and determining its operating autonomy for different power demands.

MATERIAL AND METHODS

Dynamometric tests were conducted on an agricultural tractor and an electric motor. The test with the tractor was held at the Technology Center of Machinery and Agricultural Mechanization from the Department of Engineering, Federal University of Lavras. It was used a tractor brand Green Horse Model 205 with an internal combustion engine (ICE) rated power of 14.9 kW at 2300 rpm. A dynamometer was used for tests of power take-off (PTO) model NEB 200, AW Dynamometer and also a volumetric fuel consumption meter, which is a graduated cylinder with solenoid valves that control the input and output flow of fuel which is measured by a level difference with respect to time. The dynamometer allows direct reading of the data of torque, speed and power. If necessary, a data acquisition system can be coupled to it(Figure 1A).

The dynamometric test of the electric motor (EM) was conducted at the Institute of Energy and Environment, University of São Paulo - IEE / USP. For this test was used a three-phase electric motor with a power output of 22 kW, connected in a drive three-phase frequency inverter that allowed change the motor speed.

The conjunct electric motor and frequency inverter (EM-FI) was tested in an electrical dynamometer brake composed by an electric current generator acting as load for the tested engine, submit it to the braking which is dependent on controls and electrical loads installed in the circuit (Figure 1B). To ensure parity between the internal combustion engine (ICE) and the electric motor, the maximum power of the electric motor was limited to 15 kW to maintaining equivalence compared to the ICE.

A - Functional diagram hydraulic dynamometer

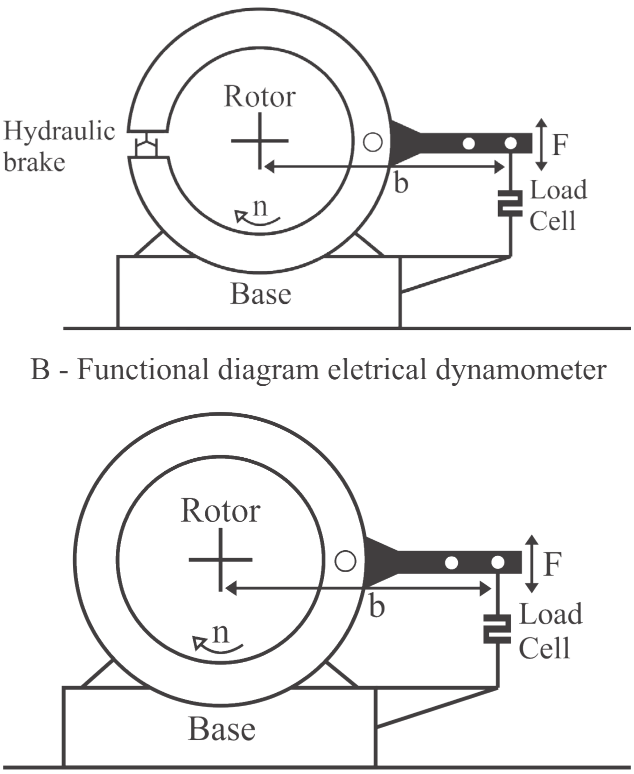

Figure 1: Scheme of a hydraulic dynamometer brake (A) and a electrical dynamometer brake (B).

For the tests in the ICE was adopted the standard NBR 1585/1996 of the Brazilian Association of Technical Standards (ABNT), which applies to the assessment of the internal combustion engine performance. For the tests in the EM- IF was adopted a methodology described by NBR 17094-2 / 2008 of the Brazilian Association of Technical Standards (ABNT), which applies to evaluating the performance of electric induction motors.

The methodology for determining the variables for the ICE and EM-IF was divided into two parts:

First acquisition of the direct variables, which could be obtained in test batteries with three repetitions: power (P), torque (T) and rotation (n) on the dynamometers. The direct variables for the ICE and EM-IF were obtained with the Equations 1 and 2.

$$T = F \times b \tag{1}$$

T - Moment of force or torque (N m)
F - force applied to the load cell (N)
B - dynamometer arm's length lever (m)

$$P = \frac{T \times n}{9,552.54} \tag{2}$$

P - Power (kW)
n - engine rotation (rpm)
9,552.54 - conversion factor

Second step consisted of determination of indirect variables that were torque reserve specific consumption (CS) and thermal efficiency of the ICE (η). The indirect variables of the ICE were calculated by Equations 3, 4 and 5.

$$\Delta T = \frac{(Tm - Tn)}{Tn} \times 100 \tag{3}$$

ΔT - torque reserve (%)
Tm - maximum torque (N m)
Tn – torque at full power (N m)

$$C_S = \frac{\rho \times Chv}{P} \times 1000 \tag{4}$$

C_S - specific fuel consumption (g kW.h^{-1})
ρ - fuel density (kg 1^{-1})
Chv - volumetric consumption (1h^{-1})

$$\eta = \frac{3,600}{C_S \times PCI} \times 100 \tag{5}$$

η - Engine thermal efficiency (%);
PCI - power net calorific value of the fuel (MJ kg-1);
3,600 - constant for unit conversion.

The indirect variables for the tests in the EM-IF were torque reserve, who was calculate with the Equation 3, and electric motor efficiency calculated by Equation 6.

$$\eta_{ME} = \frac{H_{axle}}{H_{abs}} \times 100 \tag{6}$$

η_{ME} - eletric motor efficiency (%)
H_{axle} - mechanic power at axle (kW)
H_{abs} - Eletric power absorbed by electric motor and frequency inversor (EM/FI)

The energetic cost of ICE was defined as the amount in Reais (R$) spent per kWh with produced mechanical energy. For tractor with a diesel engine ICE, the energetic cost can be defined by Equation 7:

$$CE_{ICE} = \frac{C_h \times V_c}{H_r} \tag{7}$$

CE_{ICE} - Energetic cost of internal combustion engine (ICE), (R$ kWh^{-1})
C_h - Fuel consumption schedule, (L h^{-1})
V_c - Price of the fuel (R$ L^{-1})
H_r - Reduced power (kW)

The price of the fuel was obtained by means of the average diesel prices of 24 gas stations in the southern state of Minas Gerais, which reached the average value of R$ 3.02 per liter of fuel between may, 4th and 7th, 2016.

The energetic cost of EE-FI was determined considering an electric vehicle configuration. Thus, the ME-FI set were powered by a battery pack that on the end of each test would be recharged by a charger connected to the mains. Thus, for the calculation of the energetic cost it is necessary to consider the battery charger efficiency. Thus, it was possible to deduce the equation for determining the energetic cost of the set EE (Equation 8).

$$CE_{EM} = \frac{\left(\frac{H_{abs.}}{\eta_{CB}} x V_{EE}\right)}{H_{eixo}} \tag{8}$$

CE_{EM} - energetic cost of electric motor, (R$ kWh^{-1});
H_{abs} - electric power absorbed by the ME-FIset, (kW);
η_{CB} - battery charger efficiency;
V_{EE} - price of electricity, (R$ kWh^{-1});
H_{eixo} - mechanical power in the electric engine axle (kW)

The price of electricity used in the calculation of the energy cost of the EE-FI set was obtained through a table electricity rates in rural areas made available by the National Electric Energy Agency (ANEEL, 2014) of Brazil. It was used the price charged by the energy company of Minas Gerais (Cemig), which was R$ 0.347 per kWh.

On the basis of performance of the EE-FI set, was proposed a theoretical configuration of agricultural tractor powered by electricity and characterized only as traction machine (Figure 2).

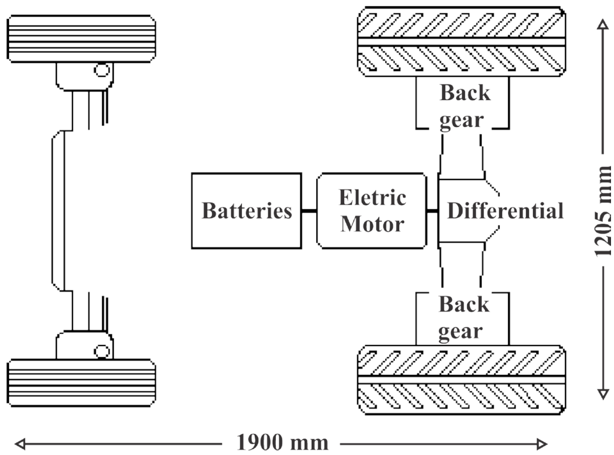

Figure 2: Diagram of theoretical configuration of the electric tractor.

The entire mass of the tractor conventional components that are unnecessary in the electric tractor model was converted into mass batteries. The purpose of this action was to keep the weight/power ratio of the tractor and to maximize their autonomy.

The mass of the ballasts of the tractor was also converted in batteries mass. Thus, in operations of higher demand for power, the mass of the batteries would be increased, resulting in weight gain. This is necessary for operations that require higher power demand. In this case also occurs autonomy gain.

As the total mass of the vehicle was calculated, a model could be defined as the number of batteries to be used. This decision was because the lithium battery has the highest energy density and power (FISHER et al. 2012) The battery adopted for the simulation presents a 48V voltage, rated current discharge 30Ah and mass 18kg. Defined the number of batteries, it was possible to calculate the electrical power available to the tractor by means of Equation 9:

$$HE_T = N_B \times V_B \times C_B \tag{9}$$

HE_T – Electric Power available on the tractor, (W);
N_B - number of batteries;
V_B- battery of voltage, (V);
C_B - battery specific capacity, (Ah).

The components used in electric tractor theoretical configuration, were defined a virtual prototype with all the considered components could be developed in order to verify some weight characteristics of the tractor as the location of its center of gravity and the weight distribution on the axles. For this, we used the CAD software (Computer-Aided Design) SolidWorks (2013).

The autonomy of the electric tractor prototype for different demands of mechanical power was calculated using a model that estimates the battery discharge time. This model is defined by Porciuncula et al. (2012) and is based on the law of Peukert, considering nonlinear properties to discharge a lithium ion (Equation 10)

$$A_{CTTE} = \frac{N_B \times \left(\dfrac{21787630,16}{\left(H_{abs} \times 270,27\right)^{1,0195}} \right)}{60} \tag{10}$$

A_{CTTE} - autonomy of the electric tractor theoretical configuration, (h);
N_B – number of batteries;
H_{abs}- electric power absorbed by the set- EM-FI, (W).

To calculate the autonomy of theoretical configuration of farm tractors in different power demands, the set EM-FI was subjected to dynamometric testing at full load (100%) and three partial loads 25, 50 and 75% of maximum power.

RESULTS AND DISCUSSION

In Figure 3, shows the torque values and power of ICE and the set EM-FI. The rotation values were defined according to their rotations obtained from the EM-IF set operating at frequencies of 30, 45, 60 and 75 Hz. For these four operating frequencies, the set EM-FI was operated at 880 rpm, 1300, 1800 and 2350 rpm, respectively. For ICE was added a fifth rotation of 2500 rpm, corresponding to the maximum motor rotation.

It could be seen that the EM-FI had set torque and power values higher than those presented by ICE across the rotation range where the two was operated machines.

The torque the set EM-FI was 36.2% higher than the ICE in the less difference between the two and 45.7% higher than in most difference shown in rotation 2300 rpm. Under these conditions, the torque values provided by the set EM-FI enable its adoption in an agricultural tractor with the characteristics of the tested model. Regarding the power the least difference in rotation was 1300 rpm, where the power of the set EM-FI was 1.53% greater than the power of the ICE. The biggest difference was 15.89% in speed of 1800 rpm.

The power values presented by the EM-FI exceed in relation to its use as a power source to the tractor used. Rodrigues et al. (2006) comparing electric motors and internal combustion engines as power sources for a tractor, achieved better results with electric motors, even with those having a 15% lower power.

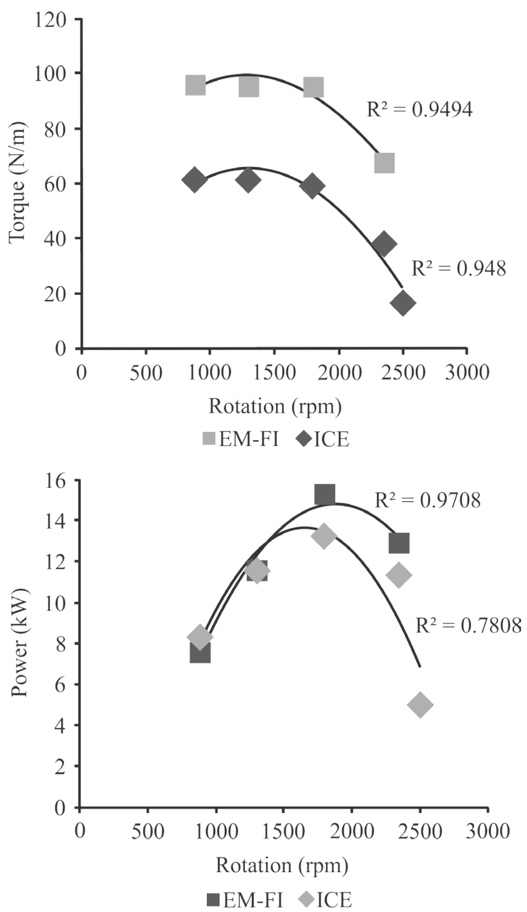

Figure 3: Curves of torque and power drawn from the results obtained in dynamometric testing of the tractor equipped with ICE and EM-FI.

The curves of efficiency and energy cost for the two engines are shown in Figure 4. The set EM-FI showed the efficiency values much higher than the figure provided by ICE throughout the rotation range. The values obtained for the set EM-FI match those supplied by the manufacturer and are also in accordance with Fedrizzi et al. (2011) who vouched that electric motors in general, frequently have efficiencies higher than 80%. The energy efficiency for ICE was 35.83% in rotation of 1800 rpm.

The ICE efficiency values are in agreement with the values observed by Barbosa et al. (2008) when testing a tractor of the 58,2kW power in one dynamometer power take-off (PTO), achieved a maximum efficiency of 38.36%. The efficiency values obtained for ICE are greater than those described by the Department of Energy of the United States - USDE (2012), according to which, considering the loss of accessories, energy efficiency diesel engine is only 18.4 %.

The EM-FI had the lowest results of cost throughout the rotation range analyzed, which reinforces the viability of the adoption of electric motors as a source of power in agricultural tractors. In addition, energy costs EM-FI showed a decreasing trend in so far as rotation is increased, unlike the ICE who presented a significant cost increase as the rotation increased.

Energy costs for the two motors can be explained by observing their energy efficiencies. While the EM-FI efficiency remained nearly constant, the efficiency of the ICE significantly changed with variation of the rotation, causing the same behavior in the cost. This common behavior of an ICE makes compulsory the use of a large number of gears in tractors, so that they can offer variation of the power and speed needed o the different agricultural operations while maintaining the ICE in the rotation range of the better energy efficiency. According Mialhe (1996), this rotation is called the motor operation range, and is situated between the maximum torque and the rotational of maximum power.

The low cost of the energetic values in the EM-FI enables its use throughout the rotation range allowing the use of a simpler mechanism of transmission of lower mass and lower cost.

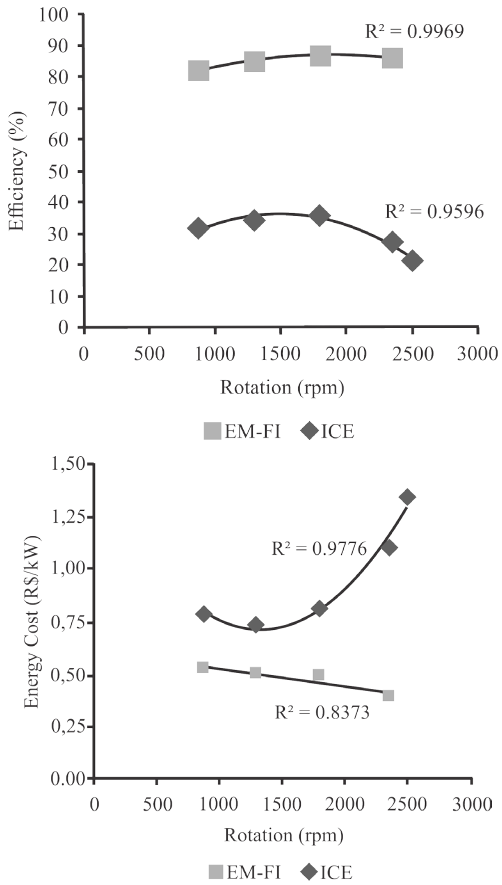

Figure 4: Curves of efficiency and energy cost drawn from the results obtained in dynamometric testing of the tractor equipped with ICE and the set EE-FI.

In Table 1 the necessary changes to the tractor to become an electric vehicle are described. These changes resulted in a reduction of 695 kg in the total mass of the vehicle and the mass was restored in the form of batteries. This value would allow the installation of 38 batteries totaling an installed power of 54.72 kW.

Table 2 shown the results of the weight/ power relation of the theoretical configuration of electric tractor compared to conventional tractor. The weight/power relation in this electric tractor theoretical configuration was 86.6 kgf kW^{-1}, and is 0.8% lower than the power/weight relation of conventional tractor used in this work.

Values of weight/power ratio of this magnitude were found in tractors with power less than 40 kW by Schlosser et al. (2005) when comparing the weight / power ratio of 106 national tractors (Brazilian tractors).

The weight distribution on the axis of theoretical configuration are was 68% on the rear axle and 32% on the front axle. This distribution is deemed appropriate for 4x2 tractors according Mialhe (1996) and was obtained by adapting the distribution of the batteryes in tractor structure shown in Figure 5.

The values obtained with 25, 50, 75 and 100% of the power EM-FI necessary for the estimate of the autonomy of electric tractor theoretical configuration submitted to different power demands are shown in Table 3. The absorbed electric power and energy efficiency could also be observed.

Table 1: Mass of conventional tractor components replaced by the mass of batteries in electric tractor theoretical configuration.

Conventional Tractor	Mass of conventional tractor component (kg)	Electric tractor	Mass of electric tractor component (kg)	Mass changed for batteries
ICE and acessories	315(1)	ME-IF	140(1)	175
gearbox	140(2)	unnecessary	0	140
Solid ballast	210(1)	Batteries weight used as ballasts	0	210
Liquid ballast (water in tires) (75%)	130(1)	Batteries weight used as ballasts	0	130
Automotive Battery	40(1)	unnecessary	0	40
Total mass of batteries (kg)				695

Table 2: Comparison of weight characteristics of the theoretical electric tractor with conventional tractor.

Characteristic	Electric tractor theoretical configuration	Conventional tractor
Weight/power relation - kgf kW^{-1} (kgf CV^{-1})	86.6 (63.6)	87.3 (64.1)
Weight in rear axle (%)	68	66
Weight in front axle (%)	32	34

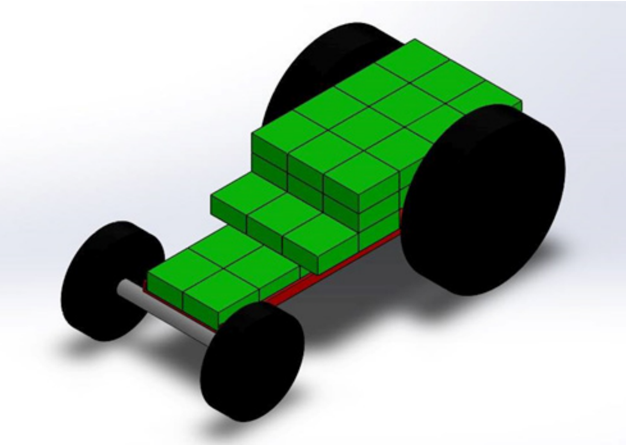

Figure 5: Simulation of weight distribution on the axis of the electric tractor theoretical configuration.

Table 3: mechanical power values, absorbed electrical power and energy efficiency obtained in the dynamometer tests with four different power levels of the set EE-IF.

Mechanic Power(kW)				
Rotation (rpm)	25%	50%	75%	100%
880	2.23	3.33	5.53	7.61
1300	3.31	5.04	8.26	11.6
1800	4.47	6.66	11.0	15.3
2300	4.74	7.41	10.2	12.9
Absorbed Electric Power (kW)				
Rotation (rpm)	25%	50%	75%	100%
880	3.24	4.40	6.88	9.29
1300	4.63	6.42	9.91	13.60
1800	5.99	8.29	12.90	17.60
2300	6.18	9.00	12.00	18.00
Energy efficiency (%)				
Rotation (rpm)	25%	50%	75%	100%
880	68.83	75.68	80.38	81.91
1300	71.49	78.50	83.35	85.29
1800	74.62	80.34	85.27	86.93
2300	76.70	82.33	85.00	71.67

Even in the most unfavorable condition with the underutilized engine with only 25% of the power the minimum energy efficiency was 68.83%. which is 100% higher than the best energy efficiency presented by ICE in tests previously.

The autonomy and power curves for different power percentage are shown in Figure 6. The set EE-FI operated of four different frequencies of 30. 45. 60 and 75 Hz. It has been conditioned to the desired power values for the four curves which were obtained at a nominal operating frequency to the set of the 60 Hz corresponding to the rotation of 1800 rpm. In this rotation range observed that curve 25% of the presented power the actual value of 29.2% of maximum power. In 50% range the real value was 43.5% of maximum power and in the range of 75% the actual value observed was 71.89% of maximum power.

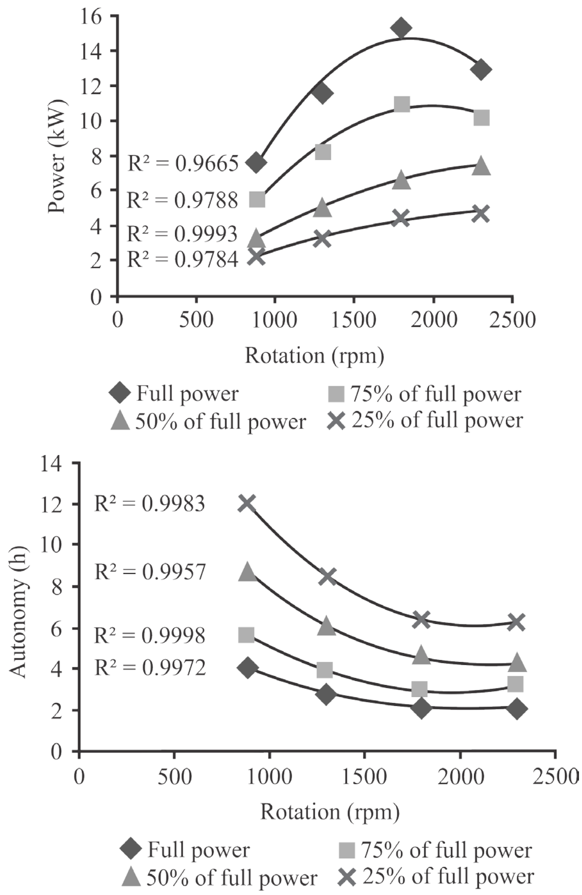

Figure 6: Power Curves and autonomy drawn from the results obtained in dynamometer testing of the set EM-FI.

The autonomy time for the power range of 25% was higher than a conventional working day of 8 hours working on rotations up to 1300 rpm. Naturally. as the power is increased. the time range reduces. At 100% power. the best autonomy time was for the rotation of 880 rpm with 4.12 h while the worst time was 2.1 h for the rotation of 2300 rpm.

Despite the low range of values presented for major power groups. these results were obtained considering that the engine was constantly subjected to high power ranges.

which in usual agricultural practice operations, it does not. Its necessary to consider the maneuver times where the defendant engine power is minimal. requiring only the displacement of the tractor-machine assembly or tractor-implement.

In addition to time maneuver which lead to a reduction in discharge velocity it is necessary to consider the different demands of power in which a tractor is submitted the according to the different agricultural operations and also the power variations that occur during the same transaction. Mialhe (1996) reported that tractors under field conditions are not requested in with more than 85 to 90% of its maximum power.

To Silveira and Sierra (2010) tractors with power of less than 30 hp work only 29.43% of the time in traction operations at speeds below 8 km h-1. which require high power. So in 70.57% of the times. tractors with power up to 30 hp. work an average of operations and low power demand and in those conditions the autonomy time would be enough for a typical working day of 8 hours.

Gamero and Benez (2009) evaluating the performance of a subsoiler to different speeds and depths found variations of up to 103.7% between the maximum and average power on the draw bar showing that even in high demand for power operations such as subsoiling. the average power demanded is less than the maximum engine power.

CONCLUSIONS

The set electric engine/frequency inverter EE-FI provides the best cost results. energy efficiency. torque and power as compared to the internal combustion engine ICE of a conventional tractor.

The electric tractor theoretical configuration presented results of autonomy to ensure operational viability. for medium power demands with lower engine speed levels. For high demand for the power. autonomy time was less than one working day of eight hours.

The results indicate great potential for the future use of electricity in the drive tractors with the evaluation of new technologies for electrical energy storage and construction of functional physical prototypes.

REFERENCES

ARMSTRONG, N. A. **The Engineered Century**. National Press Club. February 22, 2000 Available in: http://www.greatachievements.org/Object.File/Master/4/254/na_speech.pdf. Access in: September. 13. 2014.

ASSOCIAÇÃO BRASILEIRA DE NORMAS TÉCNICAS. **NBR 1585: veículos rodoviários**: código de ensaio de motores: potência líquida efetiva. Rio de Janeiro. 1996. 26 p.

BARBOSA, R. L. et al. Desempenho Comparativo de um Motor de Ciclo Diesel Utilizando Diesel e Misturas de Biodiesel. **Ciência e Agrotecnologia**, 32(5): 1588-1593, 2008.

BRASIL. Agência Nacional de Energia Elétrica. **Tarifas**: consumidores finais. Disponível em: Available in: <http://www.aneel.gov.br/area.cfm?idArea=91&idPerfil=5>. Access in: January. 12. 2014.

EDMOND, B. W. **Multifunction electric tractor**. US Patent n. EP1645456 A2. 23 Mar. 2006. Available in: http://www.google.com/patents/EP1645456A2?cl=en. Access in: January 14. 2013.

FEDRIZZI, M. C.; ALMEIDA, M. P.; MELENDEZ, T. A. Desempenho operacional de motobomba vibratória para pequenos sistemas fotovoltaicos. **Avances en Energías Renovables y Medio Ambiente**, 15(4): 13-19, 2011.

FISHER, P. et al. Electronic integration of fuel cell and battery system in novel hybrid vehicle. **Journal of Power Sources**, 220(1): 114-121, 2012

GAMERO, A. C.; BENEZ, S. H. Resultados operacionais de um subsolador com curvatura lateral (“Paraplow”) em função da velocidade e profundidade de trabalho. **Revista Energia na Agricultura**, Botucatu. 24(1): 1-16, 2009.

MIALHE, L. G. **Máquinas agrícolas**: ensaios & certificações. Piracicaba: CNPq-PADCT/TIB-FEALQ. 1996. 722p.

MOUSAZADEH, H. et al. Life-cycle assessment of a Solar Assist Plug-in Hybrid electric Tractor (SAPHT) in comparison with a conventional tractor. **Energy Conversion and Management**, 52(2011): 1700-1710, 2010.

PORCIUNCULA, C. et al. Avaliação comparativa entre o modelo elétrico Battery e os modelos analíticos Linear e Lei de Peukert. **Revista Brasileira de Computação Aplicada**, 4(1): 71-80, 2012.

RODRIGUES, D. E. et al. Micro trator agrícola adaptado com diferentes alternativas energéticas no revolvimento de café em terreiro. **Revista Ciências Técnicas Agropecuárias**, 15(4): 8-15, 2006.

SERRANO, J. M. P. Desempenho de tratores agrícolas em tração. **Revista Pesquisa Agropecuária Brasileira**, Brasília. 42(7): 1021-1027, 2007.

SILVEIRA, G. M.; SIERRA, J. G. Eficiência energética de tratores agrícolas fabricados no Brasil. **Revista Brasileira de Engenharia Agrícola e Ambiental**, 14(4): 418–424, 2010.

SCHLOSSER, J. F. et al. Análise comparativa do peso específico dos tratores agrícolas fabricados no Brasil e seus efeitos sobre a seleção e uso. **Ciência Rural**, 35(1): 92-97, 2005.

SOLIDWORKSCORPORATION. **Solidworks**. Concord. 2013. Software.

STECKEL, R. H.; WHITE, W. J. “**Engines of Growth**: Farm Tractors and Twentieth-Century U.S. Economic Welfare.” NBER Working Paper 17879. Massachusetts. March 2012.

UNITED STATES DEPARTMENT OF ENERGY. **Fuel economy**. Disponível em: <http://www.fueleconomy.gov/featv.shtml>. Acesso em: 12 fev. 2012.

UNITED STATES ENVIRONMENTAL PROTECTION AGENCY. **Office of Mobile Sources**. Non-road engines and air pollution. Available in: <http://www.epa.gov/OMS/consumer/20-nonrd.pdf>. access in: June 22. 2012.

VOLPATO, C. E. S. et al. Desempenho de Motor Ciclo Diesel Alimentado com Biodiesel de Soja (B100). **Ciência e agrotecnologia**, Lavras. 33(4): 1125-1130, 2009.

EFFECTIVENESS OF BFAST ALGORITHM TO CHARACTERIZE TIME SERIES OF DENSE FOREST, AGRICULTURE AND PASTURE IN THE AMAZON REGION

Tássia Borges Arantes
Universidade Federal de Lavras/UFLA, Departamento de Ciências Florestais/DCF, Lavras, MG, Brazil
Corresponding author: E-mail: tassiabarantes@gmail.com

Michel Eustáquio Dantas Chaves
Universidade Federal de Lavras/UFLA, Departamento de Engenharia/DEG, Lavras, MG, Brazil
E-mail: micheldchaves@gmail.com

Rafael Lemos Bastos
Universidade Federal de Lavras/UFLA, Departamento de Estatística e Experimentação Agropecuária, Lavras, MG, Brazil
E-mail: iel2702@yahoo.com.br

Luis Marcelo Tavares de Carvalho
Universidade Federal de Lavras/UFLA, Departamento de Ciências Florestais/DCF, Lavras, MG, Brazil
E-mail: passarinho@dcf.ufla.br

Marcelo Silva de Oliveira
Universidade Federal de Lavras/UFLA, Departamento de Estatística e Experimentação Agropecuária, Lavras, MG, Brazil
E-mail: marcelo.oliveira@dex.ufla.br

Abstract: Vegetation is one of the most important components of ecosystems, attracting attention and interest of the scientific community due to its undergoing constant transformation. The remote sensing systems provide data to detect, identify, map and monitor these changes. This study aimed at (1) evaluating the effectiveness of the BFAST algorithm to characterize time series of dense forest, agriculture and pasture in the Amazon region; (2) performing statistical tests in order to compare these series, and (3) fitting models to predict future values. By using the cumulative sums test, the time series of the three classes of land use were statistically different from each other, when comparing in pairs. As the series were different, the time series analysis of remote sensing data was useful in the identification and classification of different types of land use. The use of adjusted models to predict future values of the time series has proven effective for the use of Agriculture and Pasture, but not for the Forest class. It is concluded that the BFAST algorithm characterization of time series for the subsequent adjustment of models was useful for predicting harvests, considering the Agriculture use class.

Keywords: Vegetation dynamics; MODIS; Land use land cover.

Received: January, 30, 2017 - Accepted: August, 11, 2017

INTRODUCTION

The land cover has been undergoing a continuous process of change over time and space. In Mato Grosso State, in the central-west region of Brazil, the conversion of forests to agricultural use has occurred intensively in recent decades (Jasinski et al., 2005). Vegetation attracts attention and interest of the scientific community since it is considered one of the most important components of ecosystems, going through constant changes. According to Jensen (2009), much effort has been giving to the development of sensors and digital signal processing algorithms and modeling images to extract important information of the biophysical vegetation from orbital data.

In order to reduce the impact of this problem and improve policies planning, the scientific community has developed important technological projects related to the detection and indication of gradual changes in the phenological development in the field. The result has been the development of tools directly related to monitoring the productivity of crops that helps with decisionmaking in management. Many of these efforts are related to the application of remote sensing of the earth's surface, the temporal analysis of vegetation indexes in monitoring and changes detection.

The remote sensing systems provide data to detect, identify, map and monitor changes in ecosystems through multi-temporal and multi-spectral techniques (Martínez & Gilabert, 2009). Some changes occur suddenly and are caused by human activities such as forest cutting for monoculture or urban expansion, which can be easily characterized by a pair of images acquired before and after the change. On the other hand, gradual changes in the earth's surface are difficult to detect using only bi-temporal data (Coppin et al., 2004). Therefore, long and dense time series are required for an adequate characterization of incremental dynamic processes, such as the development of vegetation, seasonality, degradation and regeneration.

Furthermore, within this context, the MODIS (Moderate Resolution Imaging Spectroradiometer) has excelled in the studies of vegetation due to its daily frequency imaging of the entire globe, high geometric quality of the images and the presence of a sophisticated procedure for atmospheric correction (Justice et al., 1998). The MODIS application is directly related to vegetation through indexes, which represents advances in monitoring and generating information about the development of crops, improving the estimates by monitoring the phenological cycle and the history of changes on the Earth's surface.

The Enhanced Vegetation Index (EVI) is generated through the MODIS sensor. This vegetation index was developed to minimize constraints resulting from the saturation of an orbital image, observed mainly in vegetated areas, influenced by atmospheric effects, the substrate and the acquisition geometry (Huete et al., 2002). The index is obtained by combining the bands of red (0.62-0.67μm), near infrared (0.841 to 0.876μm), and also blue (0.459-0.479μm) (Huete et al., 1999), ranging from -1 and 1. Values close to -1 correspond to flooded areas or clouds, close to zero represent the non-existent or very sparse vegetation and close to 1 represent well-developed vegetation (Ponzoni & Shimabukuro, 2010).

Daily values of vegetative vigor are obtained due to the frequency of passage of the sensor, which enables time series analysis.

Recently, a new approach of time series processing was proposed, the BFAST (Breaks For Additive Seasonal and Trend). This method decomposes the time signature on three components: trend, seasonality and noise (Verbesselt et al., 2010a). It uses the STL procedure - Seasonal-Trend decomposition, which gives an accurate estimative, robust trend and seasonal components because of its ability to cope with extreme values or lack of values within the historical series (Verbesselt et al., 2010a, 2010b).

The BFAST was chosen for this study because of its easy implementation, through the package "bfast" free R software (R Core Team, 2016). Furthermore, it is a robust algorithm that can be applied to any type of sensor, which, in addition to decompose the series in the components of seasonality and trend, detects gradual and abrupt changes in the series.

Nevertheless, for a more detailed analysis of the dynamics of land use, it is important to know if the time signatures of different classes of land use are generated by the same stochastic process or not; meaning that these time series are statistically equal or different, assisting the identification and characterization of different land uses.

The hypothesis that guides this study is that it is possible to develop a precise model for the identification of different land uses by using time series analysis of products that are composed of vegetation indexes through the MODIS sensor, which directly assess the spectral behavior of vegetation during the course of the phenological cycle.

Therefore, this study aimed at:

a) evaluating the effectiveness of the BFAST algorithm (Breaks For Additive Season and Trend) to characterize the time signatures, based on objects from three different land use classes in the Amazon region: dense forest, agriculture and grazing, using time series of MODIS images;

b) carrying out statistical tests to compare the time series of the three land use classes;

c) fitting models to predict future values of the series.

MATERIAL AND METHODS

The study area is located in the north of Mato Grosso State, Brazil, presented in the Figure 1:

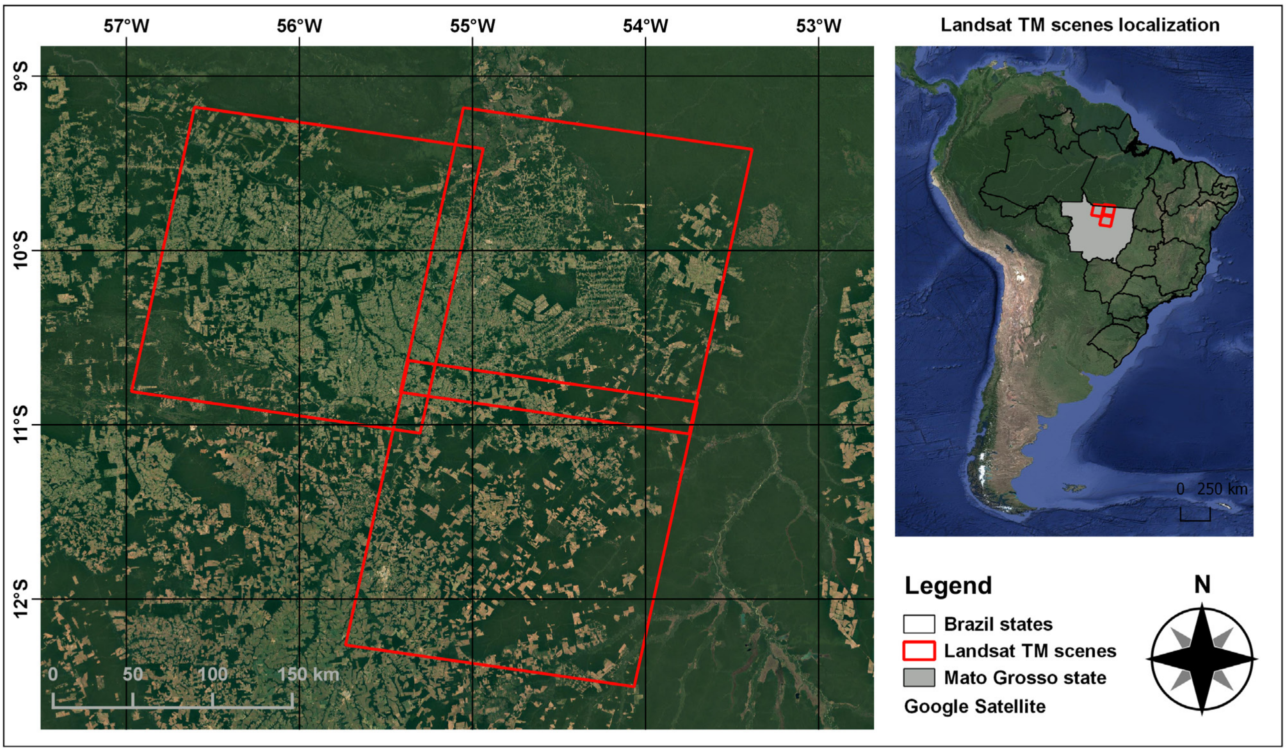

Figure 1: Study area at north of Mato Grosso, Brazil. Landsat scenes' detail, where: A) path/row 227/67, 07-31-2010; B) path/row 226/67, 07-24-2010; C) path/row 226/68, 07-31-2010.

The images from MODIS EVI index (Enhanced Vegetation Index) were acquired between September 2000 and January 2011. There was a 16-day interval between each observation (23 observations per year), with a total of 237 images. Equation 1 calculates the EVI:

$$EVI = G \frac{IVP - V}{IVP + C1xV - C2xA + L'} \tag{1}$$

where IVP represents the reflectance in near infrared, V is the red band, A is the blue band, C1and C2 are coefficients of the aerosol resistance term for red and blue respectively, L is the soil-adjustment factor and G is a gain factor.

The values adopted for the EVI were L = 1, C1 = 6, C2 = 7.5 e G = 2.5, according to recommendations proposed by Justice et al. (1998).

For the time series processing, the averages of the objects of the segmentation of Landsat TM images of the same area were used. It was selected an object for each of the following cover classes: dense forest (herein named "Forest"), Agriculture and Pasture.

The time series were analyzed using the BFAST algorithm with a package available for R software: the Gretl software (GNU General Public License, 2007) and the Statistica software (Statsoft, 2004).

The GRETL software requires monthly data. Thereby, the average of two observations of each month was considered and for the months with only one observation, 125 observations were included. From there, all other procedures were followed.

Statistical comparison between time series

For a statistical comparison between time series of the selected objects, two statistical tests were used, comparing the series in pairs, in order to determine whether they were generated by the same stochastic process or not. The tests herein used were the cumulative sums test and a series different procedures, as described below:

Cumulative sum test

Proposed by Coates & Diggle (1986), the cumulative sum test consists in using the Kolmogorov-Smirnov (KS) statistics to test a statistic based on the periodogram of the series, testing the removal of uniform distribution U(0,1). In order to perform the test, it is necessary to calculate the periodogram of the series and its reason (J). Thereby, the values of zi, cj e oj, are calculated with i=1,…,m e j=1,…,m-1 and are presented in Equations 2, 3 and 4:

$$z_i = \ln\left(1 + J^{-1}\right), \tag{2}$$

$$c_j = \sum_{i=1}^{j} z_i, \tag{3}$$

$$o_j = \frac{c_j}{c_m}. \tag{4}$$

Lastly, it is necessary to compare the oj distribution with the distribution U(0,1) trough the Kolmogorov-Smirnov test.

If the p-value is greater than α, the hypothesis accepted is that the same stochastic process generates the series. This test is suitable for small samples without normal distribution, since it is considered a nonparametric test (Gibbons, 1985). In this test, if the distance between the distributions is small, with only random deviations, H0 is accepted. If the cumulative distributions are very distant from one another at any point, H0 is rejected, suggesting that they are originated from different populations.

Time series comparison method

The procedure is as follows: the difference is made between the two series, verifying the existence of any trend and the seasonality of the series-difference using the Cox-Stuart and Fisher's tests, respectively (Morettin & Toloi, 2006). The next step is to verify if the waste is white noise, meaning that it is independent and identically distributed, with null average and constant variance, using the Box & Pierce test (1970).

If after checking by the above tests, the series-difference does not present any trend or seasonality and is considered a white noise, it can be concluded that the two series are considered equal (Costa & Sáfadi, 2010).

Models adjustment and predictions

In order to properly prepare time series predictions, it is necessary to fit a model to the series studied. The first step is to adjust the identification of the model made on the basis of autocorrelations and partial autocorrelations estimated to determine the values of p, q and d of the ARIMA (Autoregressive Integrated Moving Averages) (Morais, 2012). Therefore, autocorrelation of the series will be used to determine the model to be adjusted (preliminary estimates of the parameters to be adjusted). After the model adjustment, it is necessary to examine whether their errors are white noise or not, which means that the model represents the data properly (Morais, 2012). In this study, the Box-Pierce test was used.

According to Morais (2012), the prediction is denoted by $\hat{Z}_t(h)$ for a series Z_{t+h}, for h=1,2,... and the prediction error is given by $e_t = Z_{t+h} - \hat{Z}_t(h)$, which Z_{t+h} is the real value and $\hat{Z}_t(h)$ is the predicted value.

RESULTS AND DISCUSSION

Time series analysis and characterization

Firstly, a visual analysis of graphs was made. In Figure 2, it is observed decomposed series in seasonal, trend and noise components.

The Figure 3 presented, in the same scale, the seasonal component of the classes:

It can be observed from Figure 2 that for the three land use categories (Forest, Agriculture and Pasture), seasonality is constant throughout the period studied, observed in the Figure 3. The same behavior occurs for the trend component of Forest class, with a slight negative slope. In Pasture class, the trend remains constant until 2009, where there is a drop in the EVI values followed by growth, which may have been caused by fire. For the class of Agriculture, there were three turning points in the slope over the years. These "breaks" in the trend line probably occurred because it is an annual crop, with tillage operations every year.

By verifying if the variance in the data is constant, using the amplitude graph in function of the average, it resulted that there is no correlation, indicating that there is no need to apply logarithmic transformation on the data to stabilize the variance.

For statistical comparison of the series, it is necessary to verify if they are stationary, which means that there is a significant trend in the data. However, if the data is not stationary, it could go through some simple processing, such as differentiation, in order to get stationary. In this verification, the Dickey-Fuller test (unit root test) was applied at a 5% significance level.

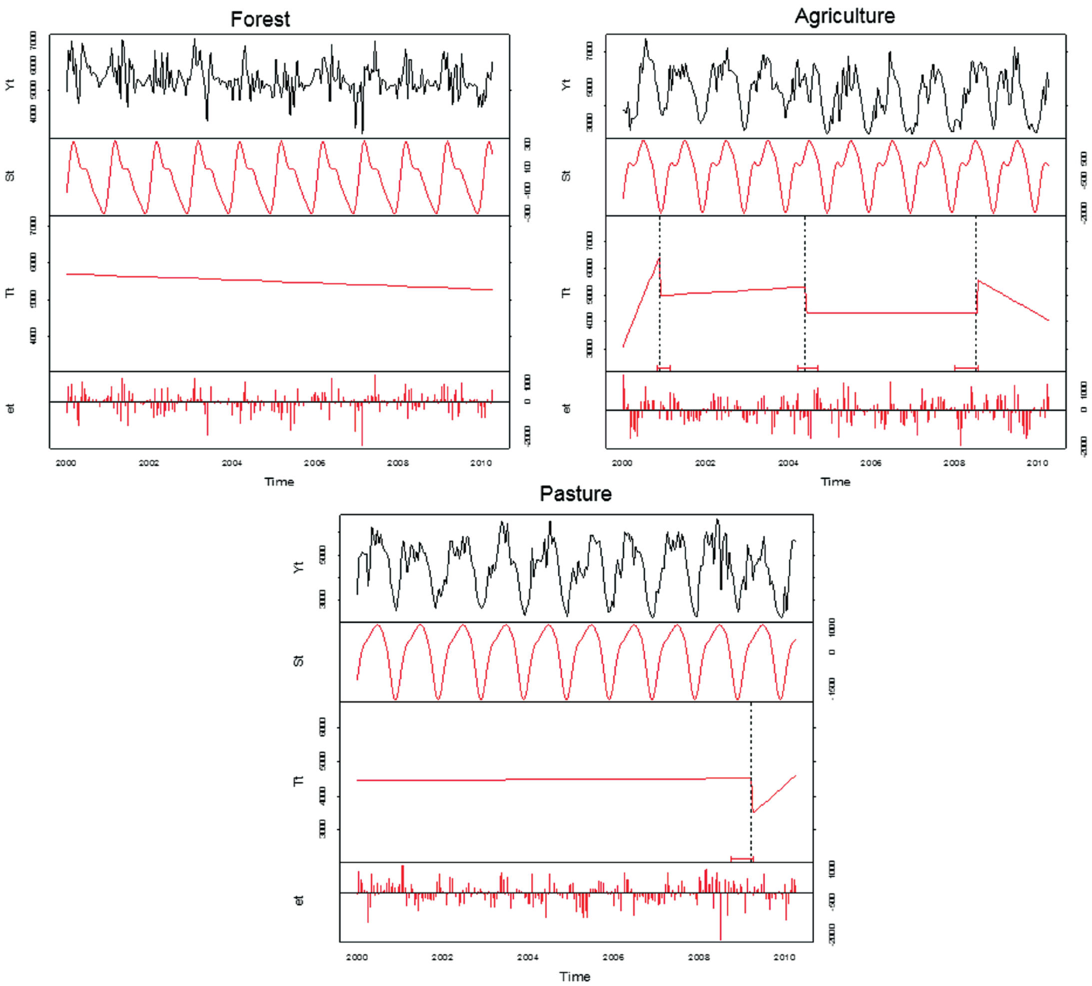

Figure 2: BFAST result for the three land use classes - Forest, Agriculture and Pasture, where Yt is the original data; St is the seasonal component; Tt is the trend component and et is the noise component.

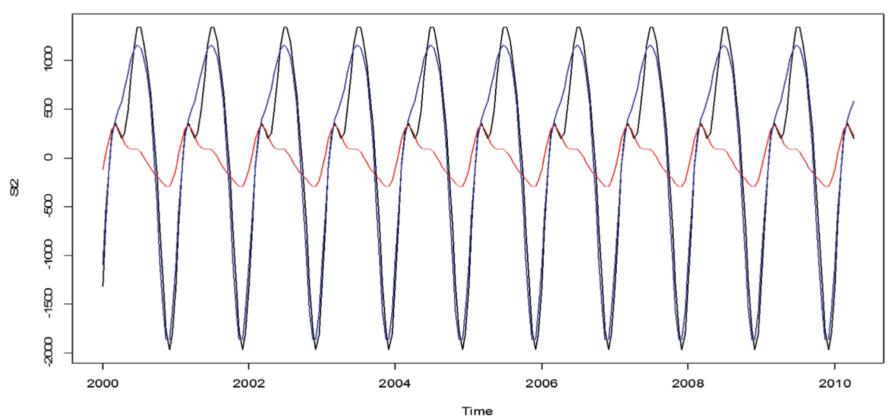

Figure 3: EVI values of the seasonal component of the three clases. Forest (red line), Agriculture (black line) and Pasture (blue line).

For the Forest class, the test showed that the series is stationary. However, for the classes of Agriculture and Pasture, the test showed that these series are not stationary. Thereby, the first-difference was applied for the two series and when the test was performed again, the data became stationary.

The periodogram of the series are shown in Figure 4. A peak is observed in period 12, approximately. Therefore, the Fisher test was applied in this period.

At 5% significance level, the test showed that there is seasonality only for the classes of Agriculture and Pasture. Therefore, a difference of 12 was applied to remove the seasonality of these series.

Comparison between series

Comparisons between the stationary series of the three different land use classes were: Forest vs. Agriculture; Forest vs. Pasture and Agriculture vs. Pasture. The results from each of the comparisons are shown next.

Forest vs. Agriculture

For the application of the cumulative sums test, the periodograms of the stationary series of Forest and Agriculture (Figure 5) were used.

In order to apply the test, the values of the periodograms of the stationary series were used, which was calculated as the ratio between the periodograms of the stationary series of Forest (numerator) and Agriculture (denominator). Thereafter, the values of de zi, cj e oj were calculated. The Kolmogorov-Smirnov test was used to compare the statistic oj of the cumulative sums test with distribution U(0,1). A p-value equals to 1.804e^{-13} were provided, rejecting the hypothesis of equality of the spectral density functions at 5% significance level. Therefore, the series of Forest and Agriculture are different and not generated by the same stochastic process.

The Cox-Stuart test was used, where the p-value was equal to 0.2522, at a 5% significance level, showing that the series difference presents

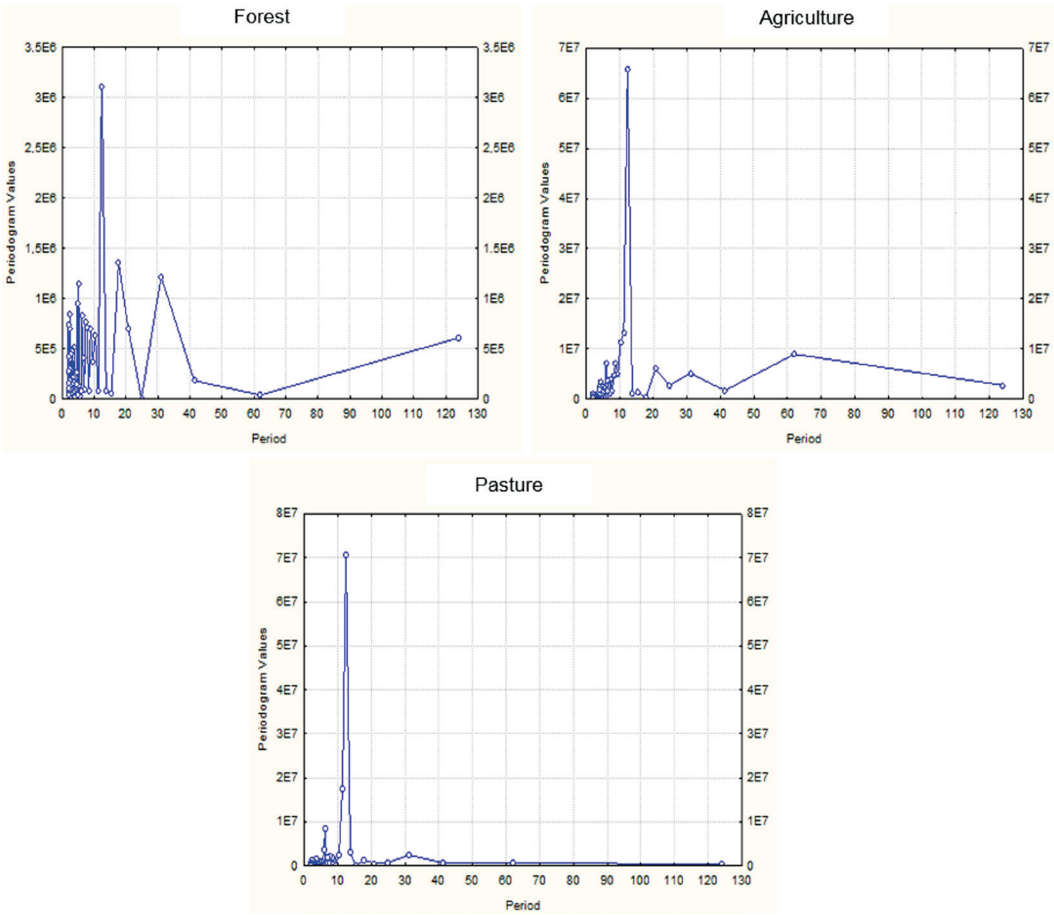

Figure 4: Periodogram of the monthly series of EVI values for the three land use classes – Forest, Agriculture and Pasture.

no trend. The Fisher's test was used to verify the seasonality of about 7 days, which did not occur.

The Box-Pierce test was used in order to verify if the difference series is considered a white noise and with $Q_{48} = 83.5710 > X^2_{48,0.05} = 62.8296$, the hypothesis that the difference series is a white noise is rejected, and therefore, the series are considered different.

Forest vs. Pasture

For the application of the cumulative sums test between Forest and Pasture, the periodogram of the stationary series of Pasture was acquired (Figure 6).

The values of de zi, cj e oj were calculated. The Kolmogorov-Smirnov test provided a p-value equals to $1.631e^{-13}$. Thereby, it rejects the hypothesis of equality of the spectral density functions at 5% significance level. Therefore, the Forest and Pasture series are different and are not generated by the same stochastic process.

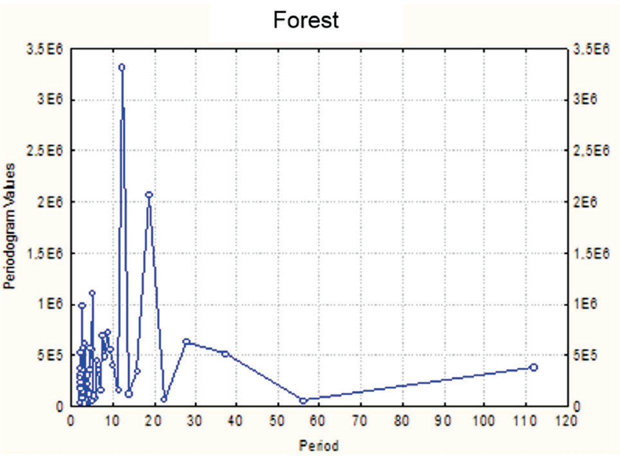

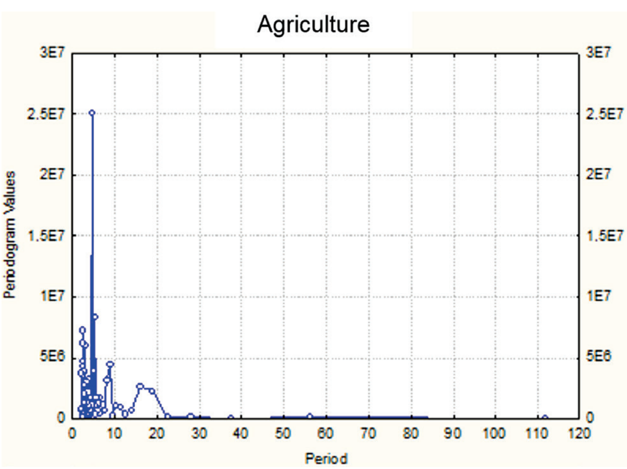

Figure 5: Stationary series periodogram of the of EVI values for the classes Forest and Agriculture.

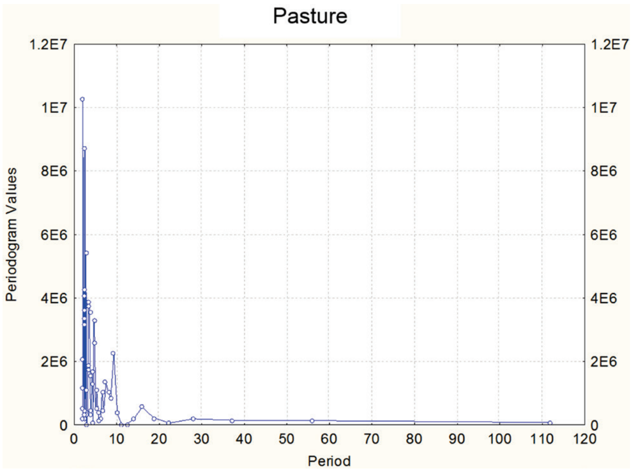

Figure 6: Stationary series periodogram of the of EVI values for the Pasture class.

Using the method proposed by Silva et al. (2000) for series comparison, it was obtained differences between the stationary series Forest and Pasture.

The Cox-Stuart test produced a p-value equal to 0.4469, indicating that there is no trend in the difference series at a 5% significance level. The Fisher's test was used to verify the seasonality of about 7 days, which did not occur.

The Box-Pierce test presented $Q_{48,0.05} = 55.6457 < X^2_{48,0.05} = 62.8296$, accepting the hypothesis that the series is considered white noise and concluding that the stationary series of Forest and Pasture are equal.

Agriculture vs. Pasture

For the cumulative sums test, the values of de zi, cj e oj were calculated. The Kolmogorov-Smirnov test provided a p-value equals to $1.887e^{-15}$. Thereby, it rejects the hypothesis of equality of the spectral density functions at 5% significance level. Therefore, the Agriculture and Pasture series are different and are not generated by the same stochastic process.

The Cox-Stuart test produced a p-value equivalent to 0.2522, indicating that there is no trend in the difference series at a 5% significance level. The Fisher's test was used to verify the seasonality of about 7 days, which did not occur.

The Box-Pierce test presented $Q_{48,0.05} = 117.4486 > X^2_{48} = 62.8296$, rejecting the hypothesis that the series is considered white noise and concluding that the stationary series of Agriculture and Pasture are different.

Model adjustment and prediction

Analyzing the correlogram and considering the orders of autoregressive operators and movable averages identified by FACP and FAC, respectively, the models were adjusted and selected according to their lower value of AIC (Akaike Information Criterion):

- Forest – ARIMA model (37, 0, 0) (AIC = 1870.889):

$$\left(1-\phi_1 B^1-\phi_2 B^{36}-\phi_3 B^{37}\right) Z_t = a_t$$

- Agriculture – SARIMA model (3,1, 0) (1, 1, 0) (AIC = 1844.990):

$$(1 - \Phi B^{12})\ (1 - \phi_1 B - \phi_2 B^2 - \phi_3 B^3)\ (1 - B^{12})\ (1 - B)\ Z_t = a_t$$

- Pasture – SARIMA model (0, 1, 1) (0, 1, 1) (AIC = 1755.026):

$$(1 - B^{12})\ (1 - B) Z_t = (1 - \Theta B^{12})\ (1 - \theta B) a_t$$

Tables 1, 2 and 3 shows the parameter estimates of the models proposed for the Forest, Agriculture and Pasture classes, respectively.

Table 1: ARIMA model parameters estimation proposed for the monthly series of EVI values for Forest class from September 2000 to January 2011.

Parameter	Estimate	Standard error
Constant	5504.790	77.839900
ϕ_1	0.184800	0.0846457
ϕ_2	0.232685	0.0909087
ϕ_3	0.234533	0.0954391

Table 2: ARIMA model parameters estimation proposed for the monthly series of EVI values for Agriculture class from September 2000 to January 2011.

Parameter	Estimate	Standard error
ϕ_1	-0.285053	0.0860709
ϕ_2	-0.292794	0.0851340
ϕ_3	-0.391918	0.0878760
Φ	-0.412260	0.0961857

Table 3: ARIMA model parameters estimation proposed for the monthly series of EVI values for Pasture class from September 2000 to January 2011.

Parameter	Estimate	Standard error
θ	-0.858831	0.0466562
Θ	-0.719185	0.0748421

Box-Pierce was applied to each model, giving the following results:

- Model (1): $Q(48) = 29.6525 < \mathcal{X}^2_{45,0.05} = 61.6562$
- Model (2): $Q(48) = 52.0206 < \mathcal{X}^2_{38,0.05} = 60.4809$
- Model (3): $Q(48) = 27.5562 < \mathcal{X}^2_{46,0.05} = 62.8296$

Therefore, all models were well adjusted. Figure 7 shows the residues autocorrelation.

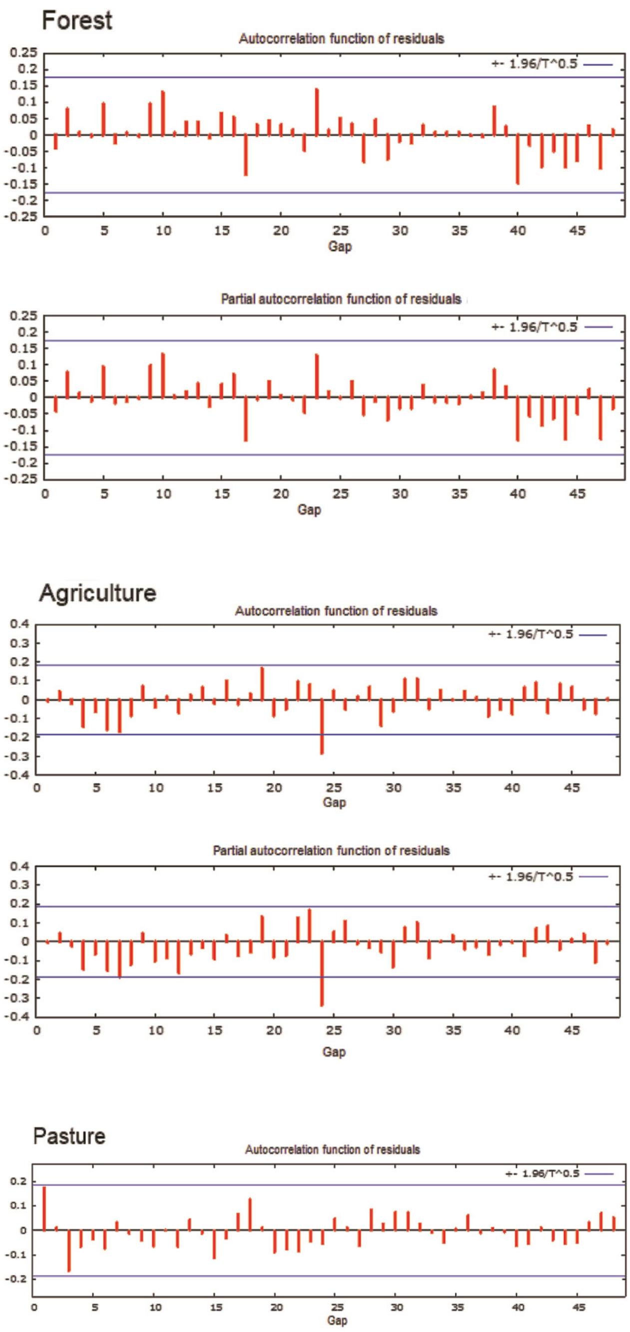

Figure 7: Autocorrelation (fac) and partial autocorrelation (facp) functions of the residuals of the models adjusted for the series of the three land use classes - Forest, Agriculture and Pasture.

The predictions were made from February 2011 to January 2012 for all land use classes, as shown in Figure 8.

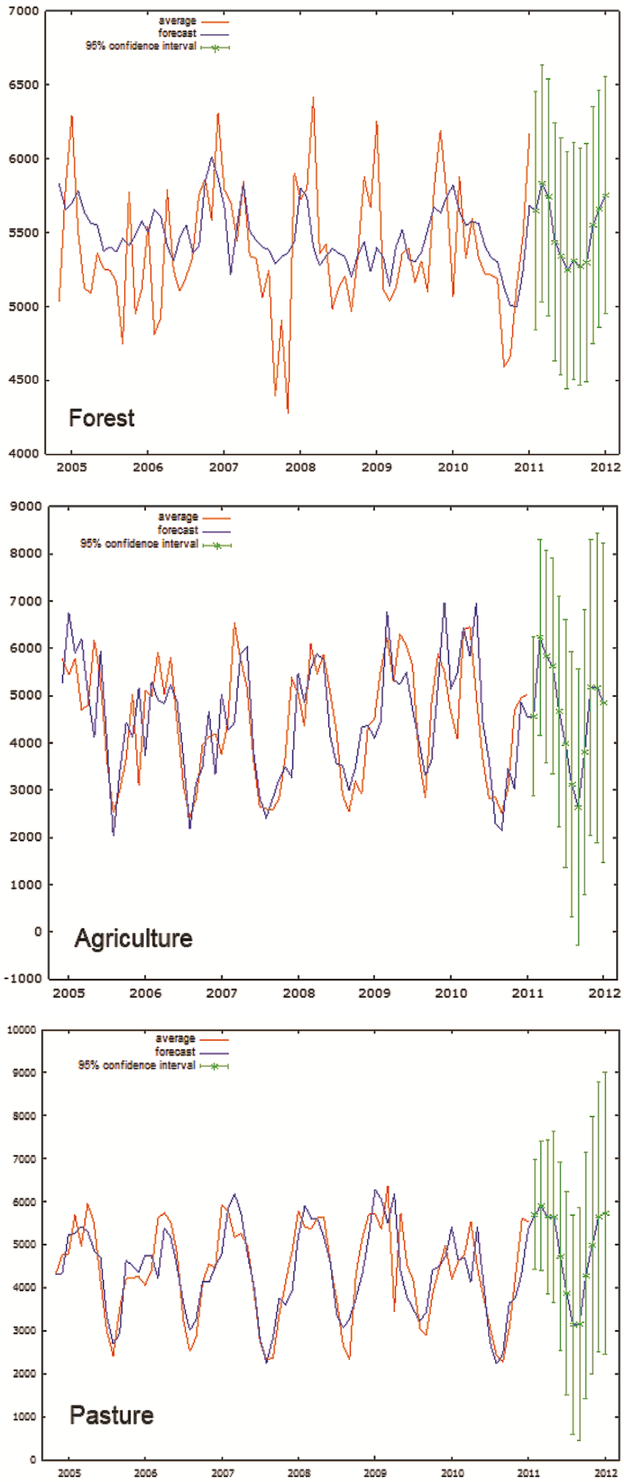

Figure 8: Observed and estimated series values according to models (1), (2) and (3) for the EVI values for the three land use classes - Forest, Agriculture and Pasture - respectively, until January 2011 and predicted values between February 2011 and January 2012.

From Figure 8, it was observed that Forest class model did not captured the real values of the series, but for the series of Agriculture and Pasture classes, the models were adequate.

CONCLUSIONS

The objectives of this study were achieved.

The BFAST algorithm was useful in characterizing the time series, allowing the observation of any changes (or not) both for the seasonal and the trend component. Using the procedure for comparing the series, only the Forest and Pasture classes showed the same behavior, statistically. However, using the cumulative sums test for comparison, the time series of the three land use classes were statistically different from each other, when compared in pairs. Therefore, as the series were different, the temporal analysis of remote sensing data was useful in the identification and classification of different types of land use.

The use of adjusted models to predict future values of the time series were effective for Agriculture and Pasture, but not for the Forest class. It is noteworthy that there is a saturation point of the values of the EVI index in areas of dense forest, which is a likely explanation for the failure of predicting future values of the time series.

It can be concluded that using the BFAST algorithm to characterize time series for subsequent adjustment models may be useful for predicting crop yields, considering the use of Agriculture class. Future research ought to be conducted with a larger number of data and locations, in order to better characterize and differentiate the types of land use.

ACKNOWLEDGEMENTS

This research project was supported by FAPEMIG and CAPES.

REFERENCES

BOX, G. E. P.; PIERCE, D. A. Distribution of Residual Autocorrelations in Autoregressive-Integrated Moving Average Time Series Models. **Journal of the American Statistical Association**, v. 65, n. 332, p. 1509–1526, 1970.

COATES, D. S.; DIGGLE, P. J. Tests for comparing two estimated spectral densities. **Journal of Time Series Analysis**, Clevedon, v. 7, n. 1, p.7-20, 1986.

COPPIN, P.; JONCKHEERE, I.; NACKAERTS, K.; MUYS, B. Review ArticleDigital change detection methods in ecosystem monitoring: a review. **International Journal of Remote Sensing**, v. 25, n. 9, p. 1565-1596, 2004.

COSTA, F. M.; SÁFADI, T. Statistical comparison of two series of particulate matter (PM10) in the city of São Paulo. **Rev. Bras. Biom**. São Paulo, v. 38, n. 3, p. 23-38, 2010.

GIBBONS, M. R.; FERSON, W. Testing asset pricing models with changing expectations an unobservable market portfolio. **Journal of Financial Economics**. v. 14, n. 2, p. 217-236, 1985.

GNU GENERAL PUBLIC LICENSE. Version 3, 29. Copyright (C) 2007 Free Software Foundation, Inc. <http://fsf.org/> June 2007.

HUETE, A., et al. A light aircraft radiometric package for MODL and Quick Airborne Looks (MQUALS). **Earth Observations**, p. 22–25, 1999 (NASA/GSFC).

HUETE, A., et al. Overview of the radiometric and biophysical performance of the MODIS vegetation indices. **Remote Sensing of Environment**, v. 83, n. 1-2, p. 195-213, 2002.

JASINSKI, E.; MORTON, D.; DEFRIES, R.; SHIMABUKURO, Y.; ANDERSON, L.; HANSEN, M. Physical Landscape Correlates of the Expansion of Mechanized Agriculture in Mato Grosso, Brazil. **Earth Interactions**, v. 9, n. 16, p. 1–18, 2005.

JENSEN, J. R. **Sensoriamento Remoto do Ambiente: uma perspectiva em Recursos Terrestres**. Traduação de J. C. N. Epiphanio. São José dos Campos, SP: Parênteses, 2009. 598 p. (Prentice Hall Series in Geographic Information Sciennce) Tradução de: Remote Sensing of the environment: na earth resource perspective.

Justice, C. O. et al. The Moderate Resolution Imaging Spectroradiometer (MODIS): Land Remote Sensing for Global Change Research. **IEEE Transactions on Geoscience and Remote Sensing**, v. 36, n. 4, 1998.

MARTÍNEZ, B.; GILABERT, M. A. Vegetation dynamics from NDVI time series analysis using the wavelet transform. **Remote Sensing of Environment**, v. 113, n. 9, p. 1823–1842, 2009.

MORAIS, T. S. T. **Estudo temporal do nível médio do mar em diferentes oceanos**. 109 p. Dissertação (Mestrado em Estatística e Experimentação Agropecuária). Universidade Federal de Lavras, Lavras, MG, 2012.

MORETTIN, P. A.; TOLOI, C. M. C. **Análise de séries temporais**. 2.ed. São Paulo: E. Brucher, 2006. 538p.

PONZONI, F. J.; SHIMABUKURO, Y. E. **Sensoriamento Remoto no Estudo da Vegetação**. ed. São José dos Campos: Parêntese, 2010. 128 p.

R CORE TEAM R: **A language and environment for statistical computing**. R Foundation for Statistical Computing, Vienna, Austria. ISBN 3-900051-07-0, URL http://www.R-project.org/. 2016.

SILVA, R. B. V.; FERREIRA, D. F.; SÁFADI, T. Modelos de séries temporais aplicados à série dos índices de preços ao consumidor na região de Lavras, MG, no período de 1992 a 1999. **Organizações Rurais e Agroindústriais**, Lavras, v. 2, n. 2, p. 44-55, 2000.

STATSOFT, Inc. **STATISTICA** (data analysis software system), version 7. www.statsoft.com. 2004.

VERBESSELT, J.; HYNDMAN, R.; NEWNHAM, G.; CULVENOR, D. Detecting trend and seasonal changes in satellite image time series. **Remote Sensing of Environment**, v. 114, n. 1, p. 106–115, 2010a.

VERBESSELT, J.; HYNDMAN, R.; NEWNHAM, G.; CULVENOR, D. Phenological change detection while accounting for abrupt and gradual trends in satellite image time series. **Remote Sensing of Environment**, v. 114, n. 12, p. 2970-2980, 2010b.

DYNAMIC ANALYSIS OF A FLARE TOWER IN OFF-SHORE PLATFORMS

Tomaz de Paula Drumond
Universidade Federal de Minas Gerais/UFMG, Escola de Engenharia, Belo Horizonte, MG, Brazil
E-mail: tomdrud@ufmg.br

Daniel Nelson Maciel
Universidade Federal do Rio Grande do Norte/UFRN, Lagoa Nova, Natal, RN, Brazil
E-mail: dnmaciel@ect.ufrn.br

Marcelo Greco
Universidade Federal de Minas Gerais/UFMG, Escola de Engenharia, Belo Horizonte, MG, Brazil
Corresponding author: E-mail: mgreco@dees.ufmg.br

Abstract: Since deepwater petroleum deposits were discovered in 2008, many projects of off-shore platforms were made in Brazil. Therefore, it is necessary to know better the behavior of structural elements that are used on these platforms, both under static and under dynamic conditions. The present work deals with the dynamic analysis of a flare tower, which is a truss structure attached to these platforms, where gases with no industrial application are burned. As a result of the burn, shock waves generated during the process reach the flare tower structure, causing the occurrence of blast loads. On the present work, the behavior of the flare tower under blast loadings was analyzed. The structure was considered as a space truss due to its geometry and its joints. New flare tower dimensions were calculated and equivalent blast loading values were estimated. These values were established as initial conditions; stress and strainvalues in the finite elements are calculated. Thus, it was possible to evaluate if the structure of the flare tower would fail and the critical conditions on the structure could be identified. Results indicate that the structure is in safe conditions up to a limited period of time, due to the fatigue of materials.

Keywords: Explosion effects; Nonlinear analysis; Space truss.

Received: April, 27 2016 - Accepted: January, 13 2017

INTRODUCTION

Since more deepwater petroleum deposits were discovered in Brazilian coast, the process of petroleum extraction was intensified, mainly by the build of new platforms. Thus, it is necessary to make an analysis to know better the elements on the maritime units that make the petroleum extraction. Among the structures in the extraction platforms, there is the flare tower, a truss structure that supports the flare where useless gases, arising from the processing of oil, are burned. This structure is extremely high to avoid the exposure of people and others equipment to the flame located at the top of the burner and the heat generated in the production plant. During the burning process at the flare tower shock waves are generated and they affect the truss structure that supports the burner. According to Kinney and Graham (1985), the generated shock waves are essentially immaterial andare generated by sudden releases of energy that occur during the burning process.

The support structure can be characterized as space truss due to its geometry and its joints. There are very few references available among the literature specifically dedicated to the flare tower analysis. The main available references for this kind of analysis are mainly technical standards, such as American Petroleum Institute (2007); TNO PrinzMauritz Institute (1997); Gilmer et al. (2003). One of the few papers available among the literature regarding this issue, Singhal (1989), is dedicated to analyze the radiations and the noise caused by flaring of the produced gas. According to Singhal (1989), the stack-enclosed flare system is studied, considering steady-state analysis and null wind velocity. This hypothesis is coherent, once the wind effect is classified as an exceptional loading for the flare tower design. The results obtained from the analysis confirms the heat radiation levels are below the allowable limits, but the author points that for prolonged exposures these limits must be reviewed. Regarding explosion analysis, Cluttera, Mathisb and Stahl (2007) states that the blast pressure from an open-field explosion event can be estimated with accepted analytical expressions. In this paper Cluttera, Mathisb and Stahl (2007), a numerical formulation is used to model the explosion effects and for the material nonlinearity it was considered an elastoplastic constitutive model for the elements.

According to Fallah and Louca (2007), the pressure-impulse (P-I) diagrams are commonly used in the preliminary design of protective structures to establish safe response limits for given blast-loading scenarios. This P-I diagram is related with a resistance function. The curve obtained from the resistance function presents an elastic-plastic-hardening or softening behavior that can be simplified as bilinear. The area under the curve is related with the P-I. The obtained results have shown that displacement time histories of the proposed analytical models are in good agreement with dynamic results obtained from finite elements analysis.

In the paper of Jia (2011) a structure similar to the flare tower was analyzed under dynamic wind effects (without blast explosion loading). The analyzed structure, called flare boom, is a type of inclined space truss built with tubular elements of stainless steel. The author proves that the wind effects acting on this type of structure can induces the fatigue of structural materials, considering both geometrical, material and load nonlinearities.

Repetto and Solari (2001) developed a probabilistic approach to evaluate the fatigue life of slender vertical structures, such as the flare tower. The authors have pointed to the importance of oscillatory behavior of the stress fields among the structural elements, when subjected to transient loads, and its relation with fatigue. This paper supplies relevant information for the comprehension of the physical phenomenon and the applications to the structural engineering.

The space truss, such as the flare tower, is a structure typically used in situations involving large displacements. When the displacements generated by an action reach a certain level, the structure geometry has a nonlinear behavior in which its stiffness changes due to new internal efforts. Thus, the structure will have two different configurations, the initial and the deformed, which must be taken into account when a project is designed. In these cases, it is not possible to make a superposition of the effects involved due to the difference between these different configurations. It is necessary then to rewrite the equilibrium equations in terms of the deformed configuration. A commonly used solution is done by the linearization of the equilibrium equations, applying algorithms with iterative corrections that use an appropriated convergence criterion.

In the present paper, dynamic actions arising from the impact of shock waves on the flare tower structure during the burning process that occurs inside it is simulated. To formulate the nonlinear kinematics involved in a space truss, the methodology presented in Greco et al. (2012) was used. In this methodology, the Lagrangian description, which considers a fixed reference in space to analyze the structure positions during a certain period of time, is adopted. Firstly, the numerical formulation will be developed for static analysis and in the sequence for the dynamic analysis.

The objective of the paper is to identify the failure mechanism of a flare tower topology and establish its safe conditions.

MATERIAL AND METHODS

The numerical formulation is developed here applying the principle of minimum potential energy. For the static analysis, the total potential energy Π is written in terms of the total strain energy Ut, and in terms of the potential energy of the applied forces, expressed as a function of the applied external forces F and the set of nodal positions X, as shown in Equation (1). Non-conservative forces that realize work could be considered in this functional.

$$\Pi = U_t - FX \tag{1}$$

According to the material elastoplastic constitutive model, the total strain energy U_t is written in Equation (2) for the reference volume V in a fixed referential.

$$U_t = \int_V u dV = \int_V \int_\varepsilon \sigma d\varepsilon dV = \int_V \left(\int_\varepsilon E\varepsilon d\varepsilon - \int_\varepsilon E\varepsilon_P d\varepsilon \right) dV = \int_V \left(\frac{1}{2} E\varepsilon^2 - E\varepsilon\varepsilon_P \right) dV \tag{2}$$

where u is the specific strain energy, σ is the stress tensor, ε is the engineering strain measure, E is the Young modulus and ε_p represents the plastic effects that occur in the body.

In order to derivate the finite element formulation from Equation (1) it is necessary the geometry mapping of the analyzed structure. For the longitudinal strains, the kinematics presented in Figure 1 is parameterized as a function of the non-dimensional variable ξ, which ranges from 0 (for the initial node) to 1 (refer to the end node). Equations (3) to (5) present this kinematical mapping.

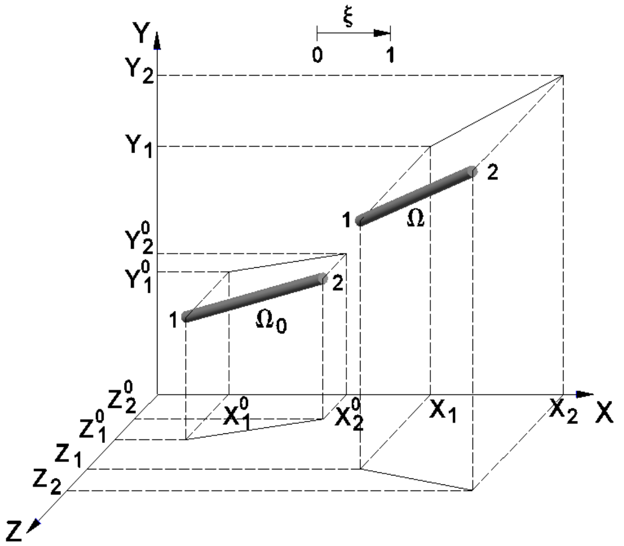

Figure 1: Space truss finite element mapping from its initial position to its deformed position.

$$x = X_1 + (X_2 - X_1)\xi \tag{3}$$

$$y = Y_1 + (Y_2 - Y_1)\xi \tag{4}$$

$$z = Z_1 + (Z_2 - Z_1)\xi \tag{5}$$

For the static nonlinear formulation, the strain measure ε that appears in Equation (2) can be written as a function of the body initial length ds_0, the body deformed length ds and the variable ξ, as shown in Equation (6).

$$\varepsilon = \frac{ds / d\xi - ds_0 / d\xi}{ds_0 / d\xi} \tag{6}$$

The Equation (2) can be integrated in terms of the cross-sectional area A constant along the finite elements' length, the element's initial length l_0 and the integral along the element's length for specific strain energy over the cross-sectional area, as shown in Equation (7).

$$U = l_0 A \int_0^1 \frac{E}{2} \varepsilon^2 d\xi = l_0 A \int_0^1 u d\xi \tag{7}$$

The total potential energy Π can be rewritten in terms of its nodal positions and conjugated forces, Equation (8), to facilitate the derivative calculations.

$$\Pi = l_0 A \int_0^1 u d\xi - F_{X1} X_1 - F_{Y1} Y_1 - F_{Z1} Z_1 - F_{X2} X_2 - F_{Y2} Y_2 - F_{Z2} Z_2 \tag{8}$$

Then Equation (8) is differentiated in terms of the directions of the degrees of freedom adopted, which can conveniently be equal to the degrees of freedom of the finite elements used in the discretization, and considered it equal to zero. Equation (9) represents the minimum potential energy expression.

$$\frac{\partial \Pi}{\partial X_i} = l_0 A \int_0^1 \frac{\partial u}{\partial X_i} d\xi - F_i = 0 \tag{9}$$

In order to obtain values for the nodal positions of the structure, iterative numerical methods can be used with suitable convergence criterion. Thus, numerical values for the body strains can be calculated.

Non linear positional formulation applied for dynamic analysis

In the case of structures subjected to dynamic loads, the equation that describes the equilibrium becomes different from that used for the static analysis. Although the formulation developed for U_t in the case of static problems remains valid, other terms appear in the definition of the total potential energy Π. There is one term K_c that refers to the kinetic energy and another term K_a that represents the energy lost due to damping, as shown in Equation (10).

$$\Pi = U_t - FX + \mathrm{K}_c + K_a \tag{10}$$

In the equations that define K_c and K_a an approach is made considering the matrix of discrete mass, according to Oliveira and Greco (2014). Therefore, these equations are represented in Equation (11) and (12).

$$K_c = \int_V \frac{\rho}{2} \dot{X}^2 dV \tag{11}$$

$$\begin{aligned} \mathrm{K}_a &= \int_V c_m \rho X \dot{X} dV - \int_V \int_{X_k} c_m \rho \frac{X\ddot{X}}{\dot{X}} dX_k dV \\ &= C X\dot{X} - C \int_{X_k} \frac{X\ddot{X}}{\dot{X}} dX_k \end{aligned} \tag{12}$$

where ρ is the element's specific mass, M is the global mass matrix, c_m is the damping coefficient, X_k represents the nodal parameters and C is the damping matrix.

To find the equilibrium positions, the minimization of the potential energy is done, now considering the terms which refer to the kinetic energy and to the energy lost due to damping. It was showed in Oliveira and Greco (2014) that the development of this minimization leads to Equation (13).

$$\frac{\partial \Pi}{\partial X} = \frac{\partial U_t}{\partial X} - F + M\ddot{X} + C\dot{X} = 0 \tag{13}$$

In the used formulation, the first term on the right side of Equation (13) is analogous to the resistance function presented in Fallah and Louca (2007). To integrate Equation (13) in time, the Newmark algorithm is used before derivate the equation for the second time considering nodal parameters. For this, the equation is written for a current instant of time S+1, as shown in Equation (14).

$$\left.\frac{\partial \Pi}{\partial X}\right|_{S+1} = \left.\frac{\partial U_t}{\partial X}\right|_{S+1} - F_{S+1} + M\ddot{X}_{S+1} + C\dot{X}_{S+1} \tag{14}$$

The Newmark time integration equations are described in Equations (15) to (17).

$$X_{S+1} = X_S + \Delta t \dot{X}_S + \Delta t^2 \left[\left(\frac{1}{2} - \beta \right) \ddot{X}_S + \beta \ddot{X}_{S+1} \right] \tag{15}$$

$$\dot{X}_{S+1} = \dot{X}_S + \Delta t (1-\gamma) \ddot{X}_S + \gamma \Delta t \ddot{X}_{S+1} \tag{16}$$

$$\ddot{X}_{S+1} = \frac{X_{S+1}}{\beta \Delta t^2} - \frac{X_S}{\beta \Delta t^2} - \frac{\dot{X}_S}{\beta \Delta t} - \left(\frac{1}{2\beta} - 1 \right) \ddot{X}_S \tag{17}$$

where β and γ are constants used to make an approximation in the Newmark time integration equations. In this work, it was adopted a constant average for accelerations in the time steps, i.e. $\gamma = 1/2$ and $\beta = 1/4$.

Replacing Equations (16) and (17) into Equation (14) one has the Equation (18).

$$\left.\frac{\partial \Pi}{\partial X}\right|_{S+1} = \left.\frac{\partial U_t}{\partial X}\right|_{S+1} - F_{S+1} + \frac{M}{\beta \Delta t^2} X_{S+1} - MQ_S + CR_S + \frac{\gamma C}{\beta \Delta t} X_{S+1} - \gamma \Delta t C Q_S \tag{18}$$

where the terms related to the past are represented by Equations (19) and (20).

$$Q_s = \frac{X_s}{\beta \Delta t^2} + \frac{\dot{X}_S}{\beta \Delta t} + \left(\frac{1}{2\beta} - 1 \right) \ddot{X}_s \tag{19}$$

$$R_S = \dot{X}_S + \Delta t (1-\gamma) \ddot{X}_S \tag{20}$$

The second derivative related of Equation (18) in terms of the current positions gives the Hessian matrix, given by Equation (21), as presented in Greco et al. (2012).

$$\left.\frac{\partial^2 \Pi}{\partial X^2}\right|_{S+1} = \nabla g\left(X^0\right) = \left.\frac{\partial^2 U_t}{\partial X^2}\right|_{S+1} + \frac{M}{\beta \Delta t^2} + \frac{\gamma C}{\beta \Delta t} \tag{21}$$

Equation (18) is nonlinear regarding spatial variables (X). To solve Equation (18) the Newton-Raphson iterative method can be applied, as described in Equations (22) and (23). Thus, the values of equilibrium positions of the structure subjected to dynamic load are calculated. From this, ΔX values are obtained, which are used to correct the new values of the nodal positions and accelerations in the current step S+1, as described in Equations (24) and (25). Then, these values are taken to Equations (15) and (16), so that the positions in the next step can be calculated.

$$g\left(X\right)\cong 0\cong g\left(X^{0}\right)+\nabla g\left(X^{0}\right)\Delta X \quad (22)$$

$$g\left(X^{0}\right)=\left.\frac{\partial U_{t}}{\partial X}\right|_{S+1}-F_{S+1}+\frac{M}{\beta\Delta t^{2}}X_{S+1}-MQ_{S}+CR_{S}+\frac{\gamma C}{\beta\Delta t}X_{S+1}-\gamma\Delta tCQ_{S} \quad (23)$$

$$X_{S+1}=X_{S}+\Delta X \quad (24)$$

$$\ddot{X}_{S+1}=\frac{X_{S+1}}{\beta\Delta t^{2}}-Q_{S} \quad (25)$$

For ΔX values of the iterative method be evaluated as sufficiently small and then move up to the next step, the stopping criterion must be defined as shown in Equation (26). When this criterion is reached, the calculated values for S+1 become the past values S.

$$\sqrt{\sum_{i=1}^{coord} g^{2}\left(X^{0}\right)}\leq TOL \quad (26)$$

Before initiate the first step, initial nodal accelerations must be calculated according to Equation (27).

$$\ddot{X}_{0}=M^{-1}\left[F_{0}-C\dot{X}_{0}-\left.\frac{\partial U_{t}}{\partial X}\right|_{0}\right] \quad (27)$$

Equivalent actions due to explosions

The process of the combustion of gases that occurs inside the flare tower violently releases a volume of compressed gas. The energy involved in this process is spread in the air, generating pressure variations and explosive waves, known as shock waves, which reach the tower surface. The behavior of the pressure that a shock wave exerts on the surface is shown in Figure 2. The wave is formed at the time of the explosion and it moves up to the surface at time t_A, when it passes immediately to exerts a high pressure on the object (overpressure peak P_{so}), which decays exponentially to a negative pressure phase known as suction region. After this suction region, there is the stabilization whit return to the ambient pressure.

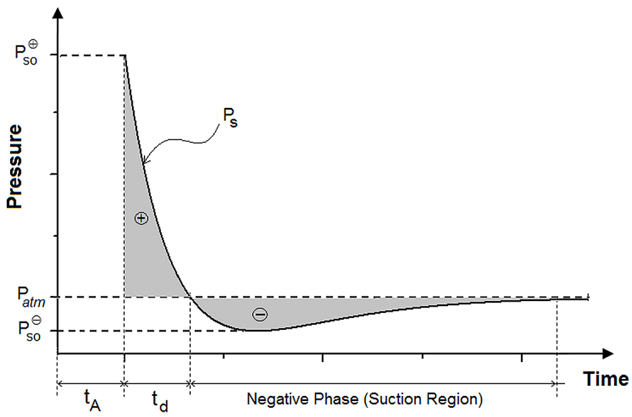

Figure 2: Transient pressure behavior for an explosive wave from the point of view of an observer or target.

The Shock Wave method presented in TNO PrinzMauritz Institute (1997) models the behavior of explosions that specifically involve gases. In this method, the values of the shock wave overpressure peak P_{so} is defined in Equation (28).

$$\frac{P_{s0}}{P_{atm}}=\phi\frac{L_{0}}{x} \quad (28)$$

where P_{atm} is the atmospheric pressure, ϕ is the reactivity level of the gas in accordance with Table 1, L_0 is the characteristic length given by Equation (29) and x is the distance from the point taken to the center of explosion.

$$L_{0}=\left[\frac{V_{0}E_{VC}}{P_{atm}}\right]^{\frac{1}{3}} \quad (29)$$

where V_0 corresponds to the volume occupied by the gas-air stoichiometric mixture calculated by Equation (30) and E_{VC} is the specific energy of the combustion.

$$V_0 = \frac{(1+5n)\cdot m \cdot R \cdot T}{Mm \cdot P_{atm}} \tag{30}$$

where m is the mass of gas, R is the universal gas constant, T is the temperature of the mixture, Mm is the molecular weight of the gas and n is the number of moles required for stoichiometric reaction O_2.

Table 1: Values of the reactivity ϕ of gases and the rate of flame spread uf, according to TNO PrinzMauritzInstitute (1997).

Reactivity	uf(m/s)	ϕ	Example of gases
Low (A)	40	0.02	Methane, Carbon monoxide, etc.
Medium (B)	80	0.06	Ethane, propane, butane, etc.
High (C)	160	0.15	Hydrogen, acetylene, ethene oxide, etc.

The duration of the positive phase t_d is defined by Equation (31).

$$t_d = \frac{L_0}{a}\left[0.456\left(\frac{a}{u_f}-1\right)+\frac{3\phi}{7}\ln\left(\frac{1+\frac{7}{3\phi}\cdot\frac{x}{L_0}}{1+\frac{1.064}{\phi}}\right)\right] \tag{31}$$

where a is the speed of sound in the air.

The function that describes the decay of the force is defined in Equation (32).

$$F(t) = \frac{P_{S0}}{S}\left(1-\frac{t}{t_d}\right)e^{\frac{-t}{t_d}} \tag{32}$$

where S is the area in which the pressure from the shock waves acts.

New and more accurate methods to evaluate accidental loads on offshore structures can be found in Hirdaris (2015) and Czujko and Paik (2015).

The analyzed flare tower structure

For the simulation of the efforts in the flare tower, the dimensions of a new structure were calculated according to the norm American Petroleum Institute API 521(2007), which establishes the tower diameter, pilot flame length, flame distortion caused by the action of winds and minimum tower height. From data obtained from Gilmer et al. (2003), it was obtained a diameter of 1.31 m and height of 65.8 m.

For the positioning of the nodes and elements that make up the flare tower, geometry similar to the tower of the Petrobras platform P-55, currently under construction to serve in Campos' Basin - RJ, was used because its comparable size to those obtained in the calculations (height: 65.8 m divided in 12 equally spaced modules; area of the base: 7.80 m; area of the top: 6.52 m). The structure was considered to be composed by 39 nodes and 108 elements arranged as shown in Figure 3. The considered elements are tubes with a diameter of 168 mm, thickness of 7.1 mm, cross-sectional area of 3.6 x 10^{-3} m², moment of inertia of 1.71 x 10^{-5} m⁴ and stainless steel composition with properties as shown in Table 2.

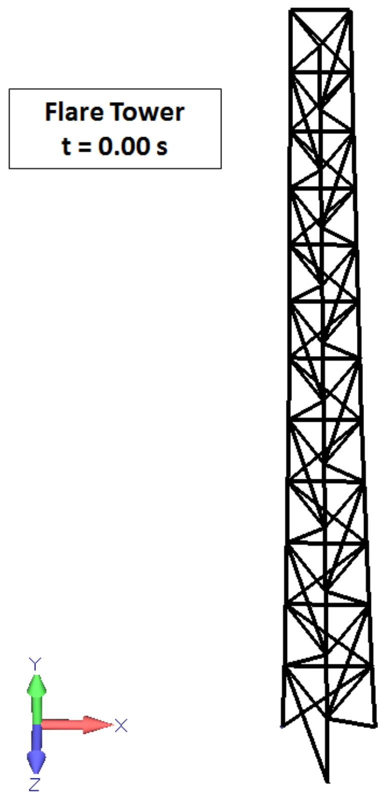

Figure 3: Flare tower used in the simulation.

Table 2: Physical properties of Stainless Steel, according to Gerdau (2015).

σ_{yield}(MPa)	$\sigma_{resistance}$(MPa)	E(GPa)	ρ(kg/m³)
355	500	200	7850

The damping values and Euler critical load for each element were also calculated. It was considered that the damping ratio equal to 1%, reasonable for applications in metal structures.

The numerical simulations were performed using an original code programmed by the authors of the paper. The initial source code presented in Greco, Ferreira and Barros (2013) was developed in Fortran language for dynamic analysis of space structures with nonlinear behavior. This code was modified to include blast loads generated by the combustion of gases at the top of flame tower.

The damping rate (ξ) presented in Equation (33) is associated to the damping coefficient (c_m) through the finite element fundamental frequency (ω).

$$\xi = \frac{c_m}{2\omega} \tag{33}$$

For the truss finite element, the fundamental frequency can be evaluated by Equation (34).

$$\omega = \frac{1}{L_0}\sqrt{\frac{E}{\rho}} \tag{34}$$

The Euler critical load as defined by Equation (35).

$$P_{CR} = \frac{\pi^2 EI}{l_o} \tag{35}$$

where *I* corresponds to the minimum inertia moment of the element. The tangent stiffness is used to caculate the critical load when plastic strains occur.

RESULTS AND DISCUSSION

To simulate the stress that appear in the tower, it was defined as tolerance in iterative stopping criterion a value equal to 10^{-8} and time steps for integration equal to 0.001s. The action of forces was divided into two phases. In the first phase, lasting 1.05s an initial and decreasing force equal to 1000 kN, distributed among the three nodes located at the top of tower, as shown Figure 4. In the second phase, it was considered a free vibration condition (without prescribed forces) so that it oscillates until return to its equilibrium position.

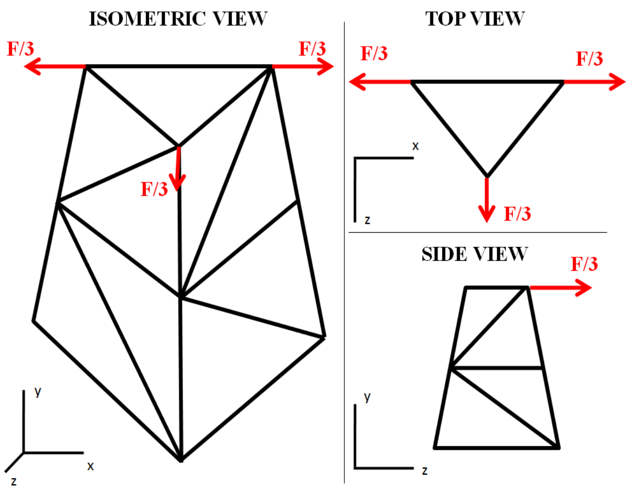

Figure 4: Distribution of the forces located at the top of the tower.

The simulation generated stress and stain results with which curves were plotted as shown in Figures 5 and 6. The responses shown that for an element located close to the medium height of the structure, the one that presented the most representative absolute values.

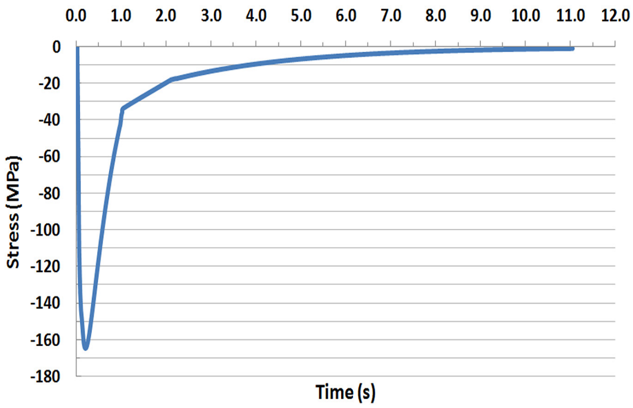

Figure 5: Normal stress transient analysis.

The complete result analysis indicates that none of the elements have reached the yield stress of 355 MPa.Thus, no plastic deformation occurred. The similarity between the stress and strain curves indicated a material linearity characteristic of the elastic behavior. As the tower was subjected to explosions permanently, this result was already expected.

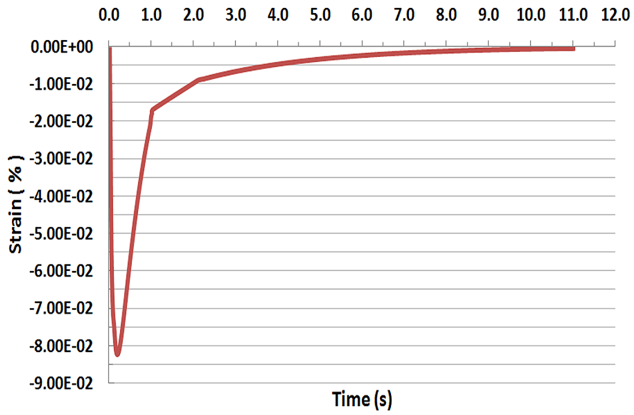

Figure 6: Normal strain transient analysis.

The obtained values also indicated that the compressive forces acting on the elements were below their Euler critical load. Therefore, it was possible to conclude that no buckling occurred in the flare tower structure.

After the simulation, the displacements values of the structure nodes were also obtained. In Figure 7, it is shown the tower in time 0.18 s, when its highest normal strain level occurred. The images of the structure in its initial (black) and deformed state (blue) were overlaid in order to facilitate the visualization of the effects generated. It can be observed that the displacements were quite small.With the displacements values it was possible to plot curves that showed the structure behavior in the x, y and z directions, as well as their respective phase figures. In Figure 8, the displacements of a node situated at the top of the flare tower are presented (in the z direction). This node presents the largest displacements among the structural nodes. In Figure 9, the phase figure for this displacement is shown.

It is noted that when the explosion finishes at time 1.05 s, the tower returns to its initial position without the occurrence of free vibration phase remarkable, probably caused by the damping ratio of 1 % that may have over-damped the structure. After reach the largest displacement of -0.37116 m, it is possible to see in Figure 9 that the structure returns to its initial position (displacement equal to zero) without oscillation. Even if it had had a free vibration phase, this fact would not occur in a real situation due to the action of a new explosion subsequent to the first, which would interrupt the return of the structure to its initial position.

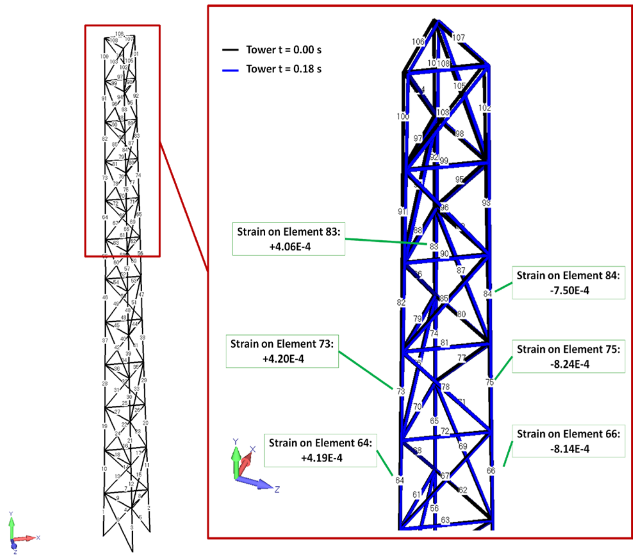

Figure 7: Tower deformed at time 0.18 s and the strain in the most representative elements.

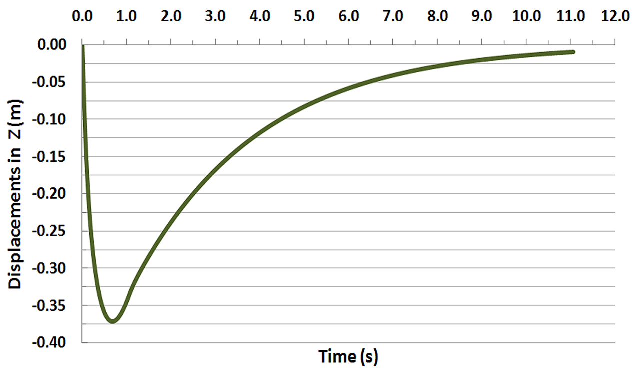

Figure 8: Transient analysis of the displacements in the z direction.

During the process of petroleum extraction, an uncountable number of explosions occur inside the flare tower as indicate the permanent pilot flame lit for most part of the time. The highest stress of 165 MPa verified during the simulation was then considered as the alternating stress that acts on the tower structure, so that an estimate could be made for the number of cycles that would indicate the tower lifetime considering fatigue. According to *Branco, Fernandes* and *Castro* (1999), the σ-n curve for the structural steel indicates that the alternating stress is below the limit of 200 MPa for the durability limit of structural steel. However, considering a lifetime of 10^8 cycles and the duration for each burst of 1.05 s, a lifetime of 3 years would be estimated. After this period, an evaluation of the maintenance in the structure would be necessary.

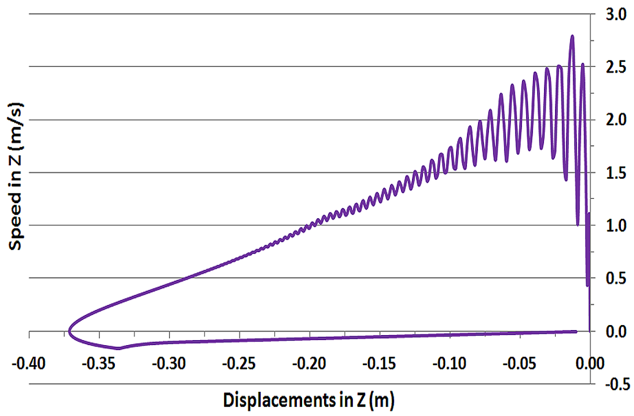

Figure 9: Phase figure for the displacements in z direction for critical top nodal point.

The values found for stresses in the structure indicated that it was projected with a good margin of safety, considering that the maximum stress verified of 84 MPa for traction and 165 MPa for compression correspond for up to 46% of the yield stress of 355 MPa for the material considered. In addition, the maximum alternating stress of 165 MPa corresponded to 83% of the limit of durability for the material fatigue, which has been indicated that the structure resists to the efforts generated on the simulation analyzed in this paper. However, it should be noted that only dynamic loads resulting from the explosions that occur inside the flare tower was considered. In a full structural analysis, exceptional efforts resulting from winds, oscillations due to tidal action in the base of the platforms and others dynamic loads should be also taken into account. Moreover, the stiffness of whole platform or ship structure must be taken into account for the full structural analysis.

Technical standard Eurocode3 (2001) limits the maximum lateral displacement in tower up to 2% of the structure height, as shown in Equation (36).

$$\delta_{MAX} = \frac{h}{50} \tag{36}$$

where h is the tower height.

This lateral displacement is limited to avoid excessive second order effects acting in the structural system. In the case of the analyzed tower, Equation (37) presents the maximum lateral displacement allowed.

$$\delta_{MAX} = \frac{65.8}{50} = 1.316m \tag{37}$$

The maximum lateral displacement obtained in the analysis (almost 0.4 m according to Figure 8) is smaller than the maximum lateral displacement allowed in the Eurocode3 standard. Thus this displacement is covered by the Eurocode3 in terms of accidental limit state.

Regarding the errors of the performed modeling, they can be classified as physical, geometrical and due to initial/boundary conditions. The physical error is related to the properties of materials (characteristic stresses, young modulus and density), besides the homogeneity of materials used in the elements. This kind of error is minor and can be considered reducing the stiffness of the elements. The geometrical error is related to imperfections due to the building process and it is more relevant as larger initial stresses were introduced in the structure. For real applications, these imperfections must be considered in the design through horizontal initial displacement on the top of the tower or through horizontal equivalent forces, as presented inthe technical procedure ABNT NBR 8880 (2008). Regarding initial conditions, several uncertainties are involved in the analysis, such as the gas constitution and the burn conditions. The adopted method is conservative regarding these uncertainties. Regarding the boundary conditions, the adopted truss idealization also presents another source of approximation, but again it is conservative regarding the structural design.

CONCLUSIONS

The flare tower has a good resistance when it is subjected to dynamic actions caused by shock waves originated during explosions that occur inside it. During the simulation, stress values obtained indicated that plastic deformation, buckling and fatigue failure do not occur. In addition, the displacements curve indicated that an accentuated free vibration phase does not occur, probably due to the damping rate of 1% considered, which may have over-damped the structure. Even if a free vibration phase were detected, it would not occur actually due to the action of a subsequent explosion that would not allow the structure to return to its initial position. The nonlinear positional formulation used in this paper was valid for simulation of dynamics efforts since it have been presented consistent results.

High temperature sources are important factors in thermomechanical analysis regarding the structures with elastoplastic behavior. It stands out the accumulation of irreversible strains because, depending on the history of the strain fields, a portion of a significant amount of heat is generated. It is emphasized the consideration of thermomechanical unidirectional coupling associated to the blast problems in which, due to high strain rates, promotes significant effects in the interaction between the mechanical and thermal response, modifying the structural behavior. Therefore, for future works, it is clear the importance of thermomechanical coupling in problems engineering, because, depending on the material, loading and initial conditions, such coupling may provide structural predominant contributions to the response. A major difficulty to model this coupling is the complex behavior of the flame and the heat propagation in the structural environment. According to Westbrook et al. (2005), the complexity of combustion models are related to different combinations of greater spatial resolution, more chemical species, a more complex turbulence model, a more sophisticated radiation model, multiple phase phenomena or moving objects.

In the current paper, truss elements were considered to model the structure. For these jointed elements, the structural analysis is more conservative and differences mainly related to natural frequencies and structural vibrations are noted. To improve the structural system modeling, the Timoshenko beam elements can be used instead of the truss elements. But with higher computational cost and, for these beam elements, some mechanical approximation still prevails (i.e. the shear stress along cross-sectional height are evaluated through a mean value). According to Hirdaris and Lees (2005), to improve the shear stress distribution, a consistent higher-order beam theory could be used. Moreover, Hirdaris and Lees (2005) presents a high order plane finite element suitable for the calculation of natural frequencies of complex free vibrating continuous systems.

ACKNOWLEDGEMENTS

The authors would like to acknowledge CNPq (National Council of Scientific and Technological Development) and FAPEMIG (Minas Gerais State Research Foundation) for financial supports, under grant numbers 302376/2016-0, 441573/2014-2 and TEC-PPM-00409-16.

REFERENCES

AMERICAN PETROLEUM INSTITUTE API 521. **Guide for pressure-relieving and depressuring systems**. API Recommended Practice. 5th ed., 2007.

ASSOCIAÇÃO BRASILEIRA DE NORMAS TÉCNICAS – ABNT NBR 8880. **Projeto de estruturas de aço e de estruturas mistas de aço e concreto de edifícios**. 2008.

BRANCO, C. M.; FERNANDES, A. A.; CASTRO, P. **Fadiga de estruturas soldadas**. 2nd ed. Lisboa: Fundação de Calouste Gulbenkian, 1999.

CLUTTERA, J. K.; MATHISB, J. T.; STAHL, M. W. Modeling environmental effects in the simulation of explosion events. **International journal of impact engineering**, 34(5): 973–989, 2007.

CZUJKO J.; PAIK, J. K. A new method for accidental limit states design of thin-walled structures subjected to hydrocarbon explosion loads. **Ships and Offshore Structures**, Special issue on Loads for Ships and Offshore Structures, 10(5): 460-469, 2015.

EUROCODE3. **Design of steel structures – S.l**. 2001.

FALLAH, A. S.; LOUCA, L. A. Pressure–impulse diagrams for elastic-plastic-hardening and softening single-degree-of-freedom models subjected to blast loading. **International journal of impact engineering**, 34(4): 823–842, 2007.

GERDAU. **Perfis estruturais Gerdau** – Informações técnicas. Brasil, 2015.

GILMER, L. K.; CAICO, C. A.; SHERRICK, J. J.; MUELLER, G. R.; LOOS, K. R. **Draft flare waste gas flow and composition measurement methodologies evaluation document**. Texas Commission on Environmental Quality, Work assignment 5. Prepared by Shell Global Solutions, Houston, Texas, 2003. Available in: https://pt.scribd.com/document/266069169/Flare-Waste-Gas-Flow-Rate. Access in: May, 12, 2017.

GRECO, M.; FERREIRA, I. P.; BARROS, F. B. A classical time integration method applied for solution of nonlinear equations of a double-layer tensegrity. **Journal of the Brazilian Society of Mechanical Sciences and Engineering**, 35(1): 41-50, 2013.

GRECO, M. et al. Comparison between two geometrical nonlinear methods for truss analyses. **Structural Engineering andMechanics**, 41(6): 735-750, 2012.

HIRDARIS, S. E. Loads on ships and offshore structures. **Ships and Offshore Structures**, 10(5): 459 (Editorial), 2015.

HIRDARIS, S. E.; LEES, A. W. A unified conforming finite element forthe vibration of thick beams and frames. **International Journal for Numerical Methods in Engineering**, 62(4): 579-599, 2005.

JIA, J. Wind and structural modelling for an accurate fatigue life assessment of tubular structures. **Engineering structures**, 33(2): 477–491, 2011.

KINNEY, G. F.; GRAHAM, K. J. **Explosive Shocks in Air**. New York: Springer-Verlag, 1985.

OLIVEIRA, F. M.; GRECO, M. Nonlinear dynamic analysis of beams with layered cross sections under moving masses. **Journal of the Brazilian Society of Mechanical Sciences and Engineering**, 37(2): 451-462, 2014.

REPETTO, M. P.; SOLARI, G. Dynamic along wind fatigue of slender vertical structures. **Engineering structures**, 23(12):1622–1633, 2001.

SINGHAL, S. N. Offshore stack-enclosed gas flares: part II - application and results. **Fire safety journal**, 15(3): 227-244, 1989.

TNO PRINZ MAURITZ INSTITUTE. **Methods for the Calculation of the Physical Effects of the escape of dangerous materials (liquid and gases) – Part II**. Yellow Book, 3rd ed., 1997.

WESTBROOK, C. K. et al. Computational combustion. **Proceedings of the Combustion Institute**, 30(1): 125–157, 2005.

PHASE SHIFT-DIGITAL SPECKLE PATTERN INTERFEROMETRY AND OPTIMIZATION FOR BONES DISPLACEMENTS PREDICTION

Rolando J. González-Peña
Universitat de València. Departamento de Fisiología, Facultad de Medicina y Odontología, Valencia, Spain
E-mail: rolando.j.gonzalez@uv.es

Ricardo Rodrigues Magalhaes
Universidade Federal de Lavras/UFLA, Departamento de Engenharia/DEG, Lavras, MG, Brazil
Corresponding author: E-mail: ricardorm@deg.ufla.br

Roberto Alves Braga Junior
Universidade Federal de Lavras/UFLA, Departamento de Engenharia/DEG, Lavras, MG, Brazil
E-mail: robbraga@deg.ufla.br

Danton Diego Ferreira
Universidade Federal de Lavras/UFLA, Departamento de Engenharia/DEG, Lavras, MG, Brazil
E-mail: danton@deg.ufla.br

Abstract: The use of phase shift-digital speckle pattern interferometry (DSPI) together with an optimization method for displacement prediction of a bone sample was evaluated. The proposed method is based on Particle-swarm Optimization (PSO) algorithm which used analytical data to obtain the bone Young's modulus for Finite Element Analysis (FEA) simulations in order to compare with experimental displacements results from DSPI. A bone sample was used in the experiments for generating the displacements by using DSPI, PSO algorithm identified the optimized Young's modulus and FEA was used to simulate displacements from the bone geometry model. Results presented good agreement between FEA and DSPI data showing error around 3%. This can be considered a potentiality of DSPI supported by optimization method and FEA for displacement prediction in bone samples.

Keywords: Particle-swarm optimization; Bone sample; Displacement measurements.

Received: May, 12, 2016 - Accepted: January, 13, 2017

INTRODUCTION

Digital Speckle Pattern Interferometry (DSPI) is a technique commonly used for micro displacement measurements in structural elements (Facchini and Zanetta (1995); González et al. (2001) and Goodman (2007)). Also, in medicine and in biomedicine fields, applications of DSPI technique are presented (Lang et al. (2004) and Román et al. (1999)) demonstrating the wide range of applications for physics properties that require sensitive approaches to access them properly.

Many investigations on the mechanical properties of bone tissue have reported different values for the modulus of elasticity (Reilly, Burstein and Frankel (1974)). The application of DSPI to determine the elastic characteristics of a bone allows the study of elastic behavior of these materials in different kind of experiments. Some related works show results for bones measurements by using optics techniques (Martinez-Celorio et al. (2010), Petzing et al. (1998) and Su et al. (2005)).

Since the biological material bring with them an intrinsic variability and heterogeneity, the outputs from the DSPI measurements require a post-processing step for adjusting results to adopt a reliable information. One post-processing approach that can be used in those cases is the particle-swarm optimization (PSO) which is based on socio-psychological principles inspired by swarm intelligence. PSO has been applied in different areas (Magalhaes et al. (2017); Jiang et al. (2007); Liu, Liu and Cartes (2008); Magalhaes, Braga Jr and Barbosa (2015); Mazhoud et al. (2013)

and Loja (2014)), including biomechanics (Hill and Banks (2014); Koh et al. (2006); Koh et al. (2009); Schutte (2005) and Yang et al. (2011)).

Therefore, this work assumed that the adoption of a PSO post-processing of the images from the DSPI application in bones displacements could improve the quality of the outcomes.

This paper is focused on applying DSPI supported by an optimization method in order to predict displacements in a bone sample by using Finite Element Analysis (FEA) (Parvitte et al. (2013)). In this case, the material property is represented by the Young's modulus in order to evaluate the use of DSPI together with optimization for displacements prediction in a bone sample.

Measurement of out of plane displacements by DSPI

Figure 1 presents DSPI components scheme for displacement measurements in the normal direction to the surface of the object. It uses a single He-Ne laser beam which is divided by a beam splitter with a semitransparent mirror with one of the two beams expanded and projected directly to the front surface of the object and reflected through a lens to produce the image in the CCD (Charge Coupled Device) camera. The other beam is the reference one which interferes with the object beam before reach the CCD camera by using a beam combiner cube. Finally, CCD camera records the interference of them and two images are recorded before and after applying the load (*P*).

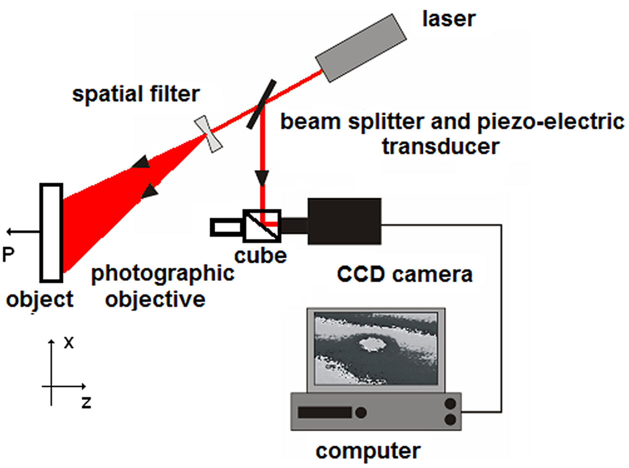

Figure 1: DSPI components scheme for displacement measurements.

Initially a reference image corresponding to the initial stage of the object without applied load is considered. Different images are successively subtracting from the reference image, resulting in a striped box. Given considerations of classical interferometry, the resulting irradiance at a point (x, y) of the image captured by the CCD camera (reference image) is given by Equation (1).

$$I_1(x,y) = I_r(x,y) + I_o(x,y) + 2|\gamma|\sqrt{I_r(x,y) I_o(x,y)} \cos\Psi(x,y) \tag{1}$$

where *Ir* (x, y) is the uniform intensity of the reference beam and I_0 (x, y) is the intensity of the object beam; $|\gamma|$ is the degree of coherence between the two beams (approximately equal to 1), which is a measure of visibility and Ψ (x, y) is the phase difference between the reference beam and the object beam at point (x, y).

When the object undergoes deformation, the new image captured by the CCD camera presents the irradiance according to Equation (2).

$$I_2(x,y) = I_r(x,y) + I_o(x,y) + 2|\gamma|\sqrt{I_r(x,y) I_o(x,y)} \cos[\Psi(x,y) + \phi(x,y)] \tag{2}$$

where φ(x, y) is the optical phase difference due to the object deformation, which is the surface where the phase shift is experienced by the speckle pattern.

When the magnitude of the final image is squared, it is obtained successive images subtraction from the reference image which is represented by Equation (3).

$$|I_1(x,y) - I_2(x,y)|^2 = \left|4 I_r(x,y) I_o(x,y) |\gamma|^2 sen^2\left[\Psi(x,y) + \frac{\phi(x,y)}{2}\right] sen^2 \frac{\phi(x,y)}{2}\right|^2 \tag{3}$$

Furthermore, the phase difference is directly related to the optical path difference of the illumination beam from the object, before and after the displacement of the point of interest. The component of the displacement outside the plane z (x, y) is related to the phase difference φ(x, y) according to Equation (4).

$$d(x,y) = \left[\frac{\lambda}{2\pi(1+\cos\theta)}\right]\phi(x,y) \tag{4}$$

where d(x,y) is the displacement and θ is the illumination angle.

In order to improve the quality of the final image, a phase-shifting process is carried out where four consecutive pictures from the object are created by adding a displacement of $\pi/2$ between them through a piezoelectric transducer coupled to a side mirror. The phase map has a phase interval between $-\pi$ and π being obtained from the Equation (5).

$$\psi(x,y) = \tan^{-1}\left[\frac{(I_4\ (x,y) - I_2\ (x,y))}{(I_1\ (x,y) - 2I_3\ (x,y))}\right] \tag{5}$$

Through a process of phase unwrapping, the phase of each point of the object is obtained and thus estimates the displacements at specified points of the object.

Considering a homogeneous, linear and isotropic beam subjected to a bending condition, the vertical displacement at centerline is represented by Timoshenko and Goodier (1970) as in the Equation (6).

$$d(x,y) = \frac{P}{2EI}(Lx^2 - \frac{x^3}{3}) \tag{6}$$

where P is the load, E is the material Young's Modulus, I is the moment of inertia, L is the beam length and x is the distance between the displacement measurement point and clamping position.

Optimization theory

By knowing experimental displacements, PSO algorithm can be applied in order to describe each particle position from the vector position in the search space from Equation (7).

$$v(t+1)\ =\ (wv(t))\ +\ (c_1 r_1(p(t)\ -\ x(t))\ +\ (c_2 r_2\ (g(t)\ -\ x(t)) \tag{7}$$

where w factor is the inertia weight, $v(t)$ is the particle's velocity at time t, $x(t)$ is the particle's current position at time t, c_1 and c_2 are constants weighting, $p(t)$ is the particle's best position, $g(t)$ vector value is the best known position found by any particle in the swarm and r_1 and r_2 are random numbers in a specific range, that normally vary between 0 and 1 (Marwala (2005)).

By applying Equation (5), the new velocity, $v(t+1)$, is used to compute the new particle's position, $x(t+1)$ as presened in Equation (8).

$$x(t+1)\ =\ x(t)\ +\ v(t+1) \tag{8}$$

Each particle moving towards the previous position tends to an optimized value.

MATERIAL AND METHODS

Experimental displacements from DSPI

In order to evaluate Young's modulus measurements by DSPI and optimization, one sample of a dried radius bone was used. Mechanical experiments (bending tests) were performed in order to provide DSPI measurements data and define the objective function to be used in the PSO algorithm. In the bending test, the bone was clamped in zero position and a static load (P) of 0.098 N was applied 92 mm far from the clamping as schematically shown in Figure 2.

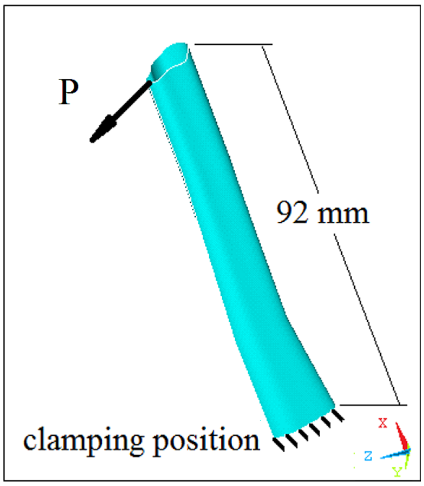

Figure 2: Sample bone drawing and loads position scheme.

Considering the non-regular geometry of the sample, it was necessary to measure the moment of inertia from different positions of the bone. A computed tomography was performed in order to measure the sample thickness at each two millimeters. These points were defined following same positions from the Finite Element model. From the cross sections measurements, a moment of inertia of 468 mm^4 was obtained. For this study, it was not taken into account the trabecular bone tissue because the experiments were provided considering pure bending. If a tensile test from a tissue is performed, it is necessary to consider the trabecular bone. Although, in long bones such as the femur, this kind of consideration is important.

A He-Ne laser beam with 632.8 nm and 45 mW was used as a source of illumination and after being projected by mirrors and expanded by a spatial filter, the beam reaches the object was illuminated at an angle around 0^o. The images were acquired by a macro (SIGMA) with a focal length of 50 mm, iris of f/16, connected to an AVT Marlin F-145B2 CCD (8bits, 1390x1040 pixels, shutter speed 1/125 s and 15fps) and the processing of phase map carried out by IDEA software (Robinson and Reid (1993)).

Optimization algorithm

In this work, the optimization algorithm was based on Visual Basic® existing code (Mccaffrey (2015)) and modified for this specific application. Basically it starts with a random value of Young's modulus to find displacements at the same points measured in the experiments. Although the bone should not be considered as an isotropic material, for simplification, it was assumed a homogeneous, linear and isotropic material in order to calculate the analytical displacements by applying the Equation (6).

The inputs for the PSO algorithm were the load, the sample length, the moment of inertia and a separated file containing the position and displacements from the experiments. The numbers of iterations, number of particles and boundaries were also required for optimization. Boundaries were considered the minimum and maximum Young's modulus assigned by the user. It was considered Young's modulus values from the literature that reported a variation between 8 and 22.8 GPa (Bosisio et al. (2007)). Based on those values, the boundaries for the PSO algorithm were established.

The algorithm also compares the two ranges of values (experimental and analytical displacements) in order to provide the difference from both ranges of values. Based on this difference, the algorithm tried a new Young's modulus value in order to minimize the error to the subsequent iteration. After the total number of iterations achieved, the algorithm stopped the analysis and indicated the estimated Young's modulus for the bone sample (Figure 3).

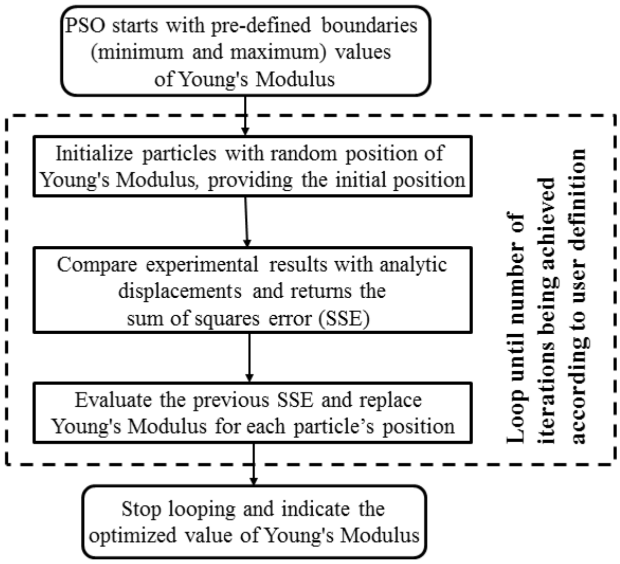

Figure 3: PSO flow chart for Young's modulus determination.

Finite Element Analysis

By knowing the estimated Young's modulus from PSO in conjunction of the scanned bone geometry, numerical simulations were able to be performed. Those data were considered as inputs for the FEA software (ANSYS®) and the expected outputs are the simulated displacements.

In order to run the Finite Element analysis, it was necessary to generate the mesh (discretized model) from the bone geometry. This process consists on the geometric model subdivision in small volumes (nodes and elements). In the case of this work, bone mesh generated 266 nodes and 144 elements (hexahedral eight node element with reduced integration). External load were applied to a node in the same position of DSPI experiments.

RESULTS AND DISCUSSION

DSPI measurement results including fringe patterns with phase-shifting and phase maps from the radius bone is shown in Figure 4.

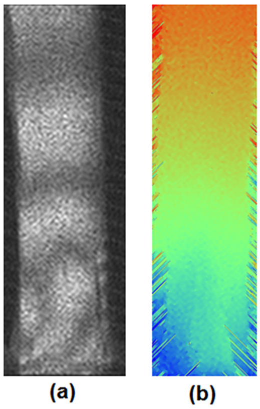

Figure 4: Fringes (a) and phase map (b) from radius bone.

From experimental data, a third order polynomial curve was obtained from DSPI measurements and it was defined as the objective function, according to Equation (9).

$$y = (-3.1\,e\text{-}9)x^3 + (8.6\text{-}7)x^2 + (1.4\,e\text{-}11)x - 2.5e\text{-}10 \quad (9)$$

where x represents the bone length and y is the DSPI displacement measurements.

In order to run the algorithm, a hundred iterations have been chosen since it was enough for the Young's modulus stabilization as observed in previous algorithm running tests. Ten particles were chosen for the analysis in the algorithm. It means that after ten PSO iteration, it was carried out over just one particle to the next iteration (best position). For this reason, Figure 5 presented the optimization result showing a total of 1000 iterations (10 particles times 100 iterations).

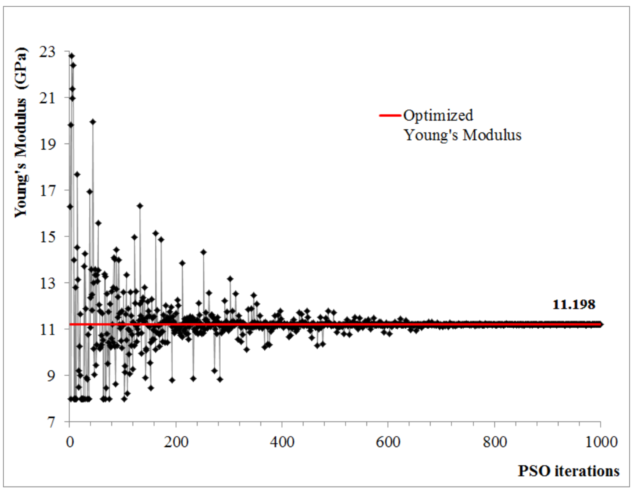

Figure 5: Optimization results for Young's Modulus estimation.

In Figure 5, it is observed the estimated Young's modulus value around 11.2 GPa. In order to certify the stability of the optimization method, wide boundary conditions were established (1 to 50 GPa), taking in consideration Young's modulus values of some less familiar bony tissues (Currey (2010)). It is noted that even changing the input parameter to a wide boundary, the results kept the same which certified the stabilization of the algorithm.

The estimated Young's modulus obtained from DSPI together with PSO was close to the literature, such as Martınez-Celorio et al. (2010) which reported 12.9 GPa by using interferometry as well. This certified the use of the estimated Young's modulus (from PSO algorithm) for displacements prediction by means of Finite Element simulations. Figure 6 presents displacements results from FEA based on the Young's modulus equals to 11.198 GPa.

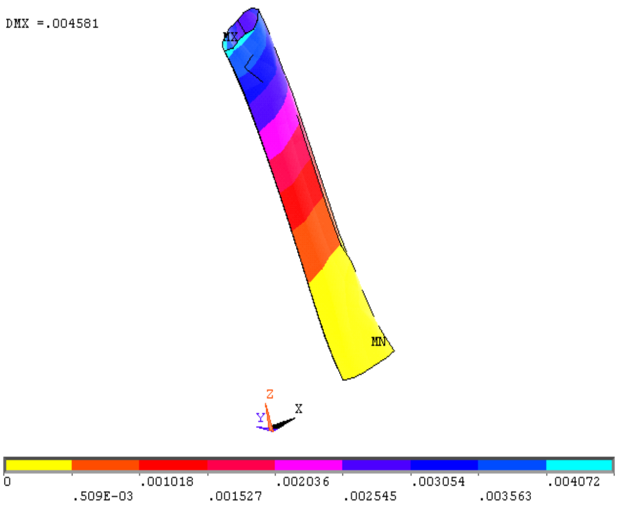

Figure 6: FEA displacements results (mm) from the bone geometry.

Figure 7 presents DSPI results (including standard deviation values) versus FEA displacements considering the simulations with estimated bone Young's modulus.

Considering the clamping position at zero mm, it is noted in the Figure 5 that from the distance around 70 mm to 92 mm, which is the total length of the bone, the difference between both curves were increased (FEA curve out of DSPI standard deviation values), although the total error was close to 3%. This increasing difference from both curves can be explained by the hypothesis that as higher as the displacements, more sensitive was the DSPI measurements. This can be considered an advantage for optical applications which require high sensitivity as reported by Braga Jr et al. (2015).

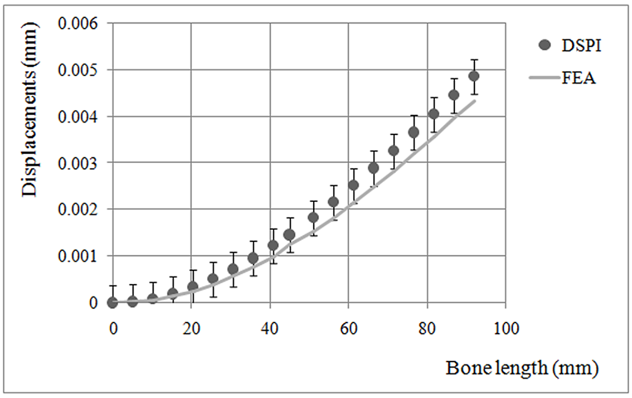

Figure 7: FEA vs.DSPI displacements results with standard deviation.

CONCLUSIONS

In this work, DSPI together with an optimization algorithm for displacements measurements of a bone sample was evaluated by comparing with FEA. Results showed 3% difference between DSPI and FEA displacements data, considering simulations with estimated Young's modulus of 11.198 GPa obtained from the PSO algorithm.

The geometry of the bone model was considered linear only in the PSO algorithm, but in bending tests and finite elements analysis, it is not. PSO algorithm was used for Young's Modulus estimation and comparison results were performed between DSPI and finite elements results.

Results also demonstrated that as higher as the displacements, more sensitive was the DSPI measurements and this can be considered an advantage for optical applications which require high sensitivity. This demonstrates the potentiality of DSPI together with optimization methods for other biomechanics applications.

ACKNOWLEDGEMENTS

This research project was partially supported by CAPES and University of Liverpool.

REFERENCES

BOSISIO, M. R. et al. Apparent Young's modulus of human radius using inverse finite-element method. **Journal of Biomechanics**, 40: 2022-2028, 2007.

BRAGA JR, R. A. et al. Maps of deformations in a cantilever beam using particle image velocimetry (PIV) and speckle patterns. **Revista Escola de Minas**, 68: 273-278, 2015.

CURREY, J. D. Mechanical properties and adaptations of some less familiar bony tissues. **Journal of the Mechanical Behavior of Biomedical Materials**, 3: 357-372, 2010.

FACCHINI, M.; ZANETTA, P. An ESPI in-plane system applied to the evaluation of mechanical characteristic of masonry. **Measurement Science and Technology**, 6: 1260-1269, 1995.

GONZÁLEZ, R. et al. Measurement of Young's modulus of cementitious materials using an electro-optic holographic technique. **Optics and Laser in Engineering**, 36: 527-535, 2001.

GOODMAN, J. W. Speckle phenomena in optics. Theory and applications. **Robert and Company Publishers**, 2007, 384 p.

HILL, I.; BANKS, S. Serial manipulator functional calibration for in vitro biomechanical testing. **Journal of Biomechanics**, 47: 289-292, 2014.

JIANG, Y. et al. Particle Swarm Optimization based on dynamic niche technology with applications to conceptual design. **Advances in Engineering Software**, 38: 668-676, 2007.

KOH, B. et al. Limitations of parallel global optimization for large-scale human movement problems. **Medical Engineering & Physics**, 31: 515-521, 2009.

KOH, B. et al. Parallel asynchronous Particle Swarm Optimization. **International Journal for Numerical Methods in Engineering**, 67: 578-595, 2006.

LANG, H. et al. Determination of the dynamics of restored teeth by 3D electronic speckle pattern interferometry. **Lasers in Surgery and Medicine**, 34: 300-309, 2004.

LIU, L.; LIU, W.; CARTES, D. A. Particle Swarm Optimization-based Parameter Identification Applied to Permanent Magnet Synchronous Motors. **Engineering Applications of Artificial Intelligence**, 21: 1092-1100, 2008.

LOJA, M. A. R. On the use of particle swarm optimization to maximize bending stiffness of functionally graded structures. **Journal of Symbolic Computation**, 61-62: 12-30, 2014.

MAGALHAES, R. R.; BRAGA JR, R. A.; BARBOSA, B.H.G. Young's Modulus evaluation using Particle Image Velocimetry and Finite Element Inverse Analysis. **Optics and Lasers in Engineering**, 70: 33-37, 2015.

MAGALHAES, R. R. et al. Application of particle swarm optimization in inverse finite element modeling to determine the mechanical behavior of the cornea. **Acta Scientiarum Technology**, 39: 325-331, 2017.

MARTINEZ-CELORIO, R. A. et al. Young's modulus measurement of the radius bone using a shearing interferometer with carrier fringes. **Optics and Lasers in Engineering**, 48: 727-731, 2010.

MARWALA, T. Finite Element Model Updating Using Particle Swarm Optimization. **International Journal of Engineering Simulation**, 6: 25-30, 2005.

MAZHOUD, I. et al. Particle swarm optimization for solving engineering problems: A new constraint-handling mechanism. **Engineering Applications of Artificial Intelligence**, 26: 1263-1273, 2013.

MCCAFFREY, J. Particle Swarm Optimization. Available at: **https://msdn.microsoft.com/magazine/hh335067**. Accessed on: May, 05, 2015.

PARVITTE, B. et al. Quantitative simulation of photoacoustic signals using finite element modelling software. Applied Physics B: **Lasers and Optics**, 111: 383-389, 2013.

PETZING, J. N. et al. The analysis of human femur and prostheses using Electronic Speckle Pattern Interferometry. **Engineering Science and Education Journal**, 7: 35-40, 1998.

REILLY, D. T.; BURSTEIN, A. H.; FRANKEL, V. H. The elastic modulus for bone. **Journal of Biomechanics**, 7: 271-276, 1974.

ROBINSON, D. W.; REID, G. T. Interferogram analysis: Digital fringe pattern measurement techniques, **Institute of Physics Publishing**, 1993, 302 p.

ROMÁN, J. F. et al. The mechanical behavior of human mandibles studied by Electronic Speckle Pattern Interferometry. **The European Journal of Orthodontics**, 21: 413-421, 1999.

SCHUTTE, J. F. Evaluation of a particle swarm algorithm for biomechanical optimization. **Journal of Biomechanical Engineering**, 127: 465-474, 2005.

SU, M. et al. Measurement of bone strain using electronic Speckle Pattern Interferometry. **Journal of Holography and Speckle**, 2: 34-39, 2005.

TIMOSHENKO, S. P.; GOODIER, J. N. Theory of Elasticity, **McGraw Hill Book Company**, 1970. 591 p.

YANG, A. et al. Computation of physiological human vocal fold parameters by mathematical optimization of a biomechanical model. **Journal of the Acoustical Society of America**, 130: 948-964, 2011.

AUTHOR GUIDELINES

1. The concepts and conclusions included in papers are of the entire responsibility of the authors.

2. Theoretical and Applied Engineering is a scientific journal edited once every two months by the Federal University of Lavras Publishing House (Editora UFLA) and UFLA Engineering Department. The journal publishes innovative contributions in engineering applications ranging from the integration of instruments, methodologies and technologies and their use in the environmental sciences, engineering and other natural sciences. Theoretical and Applied Engineering is devoted to a wide range of subfields in the engineering sciences. Articles of interdisciplinary nature are particularly welcome. The articles must be elaborated by researchers of national and international scientific communities. Submission of a manuscript to this journal requires that it has neither been published nor is under consideration for publication elsewhere. Upon acceptance for publication, authors assign to the journal full copyright of the manuscript in all languages and countries.

3. Publication process: Submitted manuscripts will be forwarded to the editorial board to be initially evaluated in terms of comparative relevance to other papers of the same area that were submitted for publication. If it is considered as relevant, the paper will be submitted to blind peer reviewers. If approved and if necessary, the manuscript may return to the correspondent author for corrections. If the corrections are not returned within the required deadline, the publication process will be automatically cancelled. Requested corrections not attended without justification may also lead to cancellation. After these revisions, the manuscript will receive corrections of scientific nomenclature, english, and references. Following these corrections, the manuscript will be edited and published.

4. Cost of publication: There is no publication costs.

5. Manuscripts must be submitted electronically (http://www.taae.deg.ufla.br/taae/index.php/TAAE), written in English, and use only conventional abbreviations and nomenclature with no abbreviations in the title. Manuscripts must be edited using the program Microsoft Word for Windows on paper size A4 (21 cm x 29.7cm), double spaced using Times New Roman font, size 12, with a 2.5 cm margin on both left and right hand side, and on upper and lower margins, heading and footnote. A letter must be sent to the Editor requesting the manuscript publication with the author's full name with no abbreviations, title degree and work address (street, number, zip code, city, state, country and e-mail). At submission, this document must be attached in the field "Cover Letter". Any further insertion, exclusion or alteration in the authors order must be informed by a document signed by all authors (including the excluded author, if the case).

6. Each manuscript must be organized in the following format: a) TITLE (capital letters) sufficiently clear; conspicuous and complete, without abbreviations and superfluous words, written in English and Portuguese. It is recommended to begin with the term that represents the most important aspect, with other terms in decreasing of importance; b) FULL NAME(S) OF THE AUTHOR(S) (without abbreviations) on the right side with one name beneath the former. The manuscript must have a maximum of 6 (six) authors; c) ABSTRACT must be written continuously in one paragraph and it must not exceed 250 words. At least, it must contain a brief introduction, objective(s) and main results, d) INDEX TERMS with 3 to 5 keywords that express the content of the paper and different from those used in the title and separated by commas; e) INTRODUCTION (including literature review and objectives); f) MATERIAL AND METHODS; g) RESULTS AND DISCUSSION (it may include tables and figures); h) CONCLUSION(S); i) ACKNOWLEDGMENT(S) (optional) with serious and clear written style, indicating the reason(s) for the recognition(s); j) REFERENCES (without citations of thesis, dissertation and/or abstracts).

7. FOOTNOTE: It must contain title degree (MS, PhD, Dr, etc), institution of work with the complete address (street, number, zip code, P. O. Box, city, state, country) and e-mail of the corresponding author.

8. TABLES: Must contain a clear and concise title, being explanatory. Tables should not contain vertical lines. Horizontal lines must separate title from the presented data and at the bottom of the table. Tables should be made on Microsoft Word (Table - Insert Table), with each value inserted in a single cell, centrally located.

9. PHOTOGRAPHS, GRAPHS, FIGURES, SYMBOLS OR FORMULAS CONTAINED IN THE PAPER SHOULD FOLLOW THE RULES BELOW:
The figures listed above must be both inserted after their citation in the text and also sent in separate files attached to the MANUSCRIPT FILES field.

10. Photographs may be in color or black and white, clear and with contrast, inserted in the text after their citation and also in a separate file, saved in extension "TIFF" or "JPEG" with resolution of 300 dpi. Press copies will only publish photographs in black and white.

11. Figures may be in color or black and white, clear and with contrast, inserted in the text after their citation and also in a separate file, saved in extension "TIFF" or "JPEG" with resolution of 300 dpi. They must be described using Times New Roman font, size 10, without bold, without a text box and arranged in order. Press copies will only publish figures in black and white.

12. Graphs must be inserted in the text after their citation. Graphs must be described preferentially in Excel, using Times New Roman font, size 10, without bold, saved in XLS extension and transformed into TIFF or JPG files with a resolution of 300 dpi.

13. Symbols and Chemical Formula must be presented using a word processor that allows editing for Adobe InDesign CS6 (ex: MathType), maintaining their original layout.

14. CITATION IN THE TEXT BY THE ALPHABETIC SYSTEM (AUTHOR-DATE)
Two authors: Alves and Silva (2014).
Three authors: Silva, Alves and Volpato (2013).
More than three authors: Volpato et al. (2014).
Note: When two authors of the same work are cited they must be separated by "and", if not included in the sentence, must be separated by ";". Other cites in the same text, must present the authors in an alphabetic order of their last names, followed by date and separated by ";": Alves (2010); Silva Junior (2011); Oliveira (2012) and Ferreira (2013).

15. REFERENCES: All references and their correct citation in the text are the responsibility of the author(s).
General information:
- Journal name must be completely written (no abbreviations) in bold .
- All the references must list the journal volume, issue (in parenthesis), initial and final pages and year of publication.
- References must be set in alphabetic order, aligned left and simple spaced in a reference and double spaced between references.

EXAMPLES (MOST COMMON TYPES).

JOURNAL PAPER:
- Up to three authors:

DRUMOND, T. P.; MACIEL, D. N. GRECO, M. Dynamic analysis of a flare tower in off-shore platforms. Theoretical and Applied Engineering, 1(1):20-30, 2017.

-More than three authors:
ARANTES, T. B. et al. Effectiveness of bfast algorithm to characterize time series of dense forest, agriculture and pasture in the amazon region. Theoretical and Applied Engineering, 1(1):10-19, 2017.

BOOK
a) Complete book:
SILVA, F. M.; ALVES, M. C. Cafeicultura de precisão. 1.ed. Lavras: Editora UFLA, 2013. 227p.
b) Book chapter with specific authors:
ALVES, M. C.; SILVA, F. M. ; OLIVEIRA, M. S. Erros de medição em topografia. In: ALVES, M. C.; SILVA, F. M. Geomática para levantamento de ambientes: base para aplicações em topografia, georreferenciamento e agricultura de precisão. 1ed. Lavras: Editora UFLA, 2016. v. 1, p.53-80.

DISSERTATION AND THESIS:
Must not be cited.

ABSTRACTS PUBLISHED IN CONGRESSES OR OTHER EVENTS:
Must not be cited.

CHECK LIST AFTER MANUSCRIPT ACCEPTANCE
a) Inform the author of the correspondence;

b) The institutional affiliation data for the footnote must be organized by: Institution/Acronym, Department/Acronym, city, state (abbreviated), country;

c) Inform the dates of receipt and approval of the article;

d) Index terms should not be contained in the title. They are separated by a semicolon. Only the first keyword starts in uppercase and after all keywords end with dot;

e) All unnumbered titles and subtitles: INTRODUCTION - MATERIAL AND METHODS - RESULTS AND DISCUSSION - CONCLUSIONS - ACKNOWLEDGEMENTS (optional);

f) Figures, Tables and Equations must be called in the text before they are presented;

g) Observe in the Figures and Tables the standardization of the data, according to English standard, regarding the use of points and commas;

h) Send separate and named images according to position in the article (Figure 1), in .JPG format and in high resolution (300 dpi);

i) Observe standards for standardization of bibliographic references in the body of the article and in the list of references at the end of the article, so that a reference is not listed that does not appear in the article or cited a reference that is not in the list of references.